Lehto, Pauli

Adaptive domain misorientation approach for the EBSD measurement of deformation induced dislocation sub-structures

Published in:
ULTRAMICROSCOPY

DOI:
10.1016/j.ultramic.2021.113203

Published: 01/03/2021

Document Version
Publisher's PDF, also known as Version of record

Lehto, Pauli

Adaptive domain misorientation approach for the EBSD measurement of deformation induced dislocation sub-structures

Published in:
ULTRAMICROSCOPY

DOI:
10.1016/j.ultramic.2021.113203

E-pub ahead of print: 01/03/2021

Document Version
Publisher's PDF, also known as Version of record

Ultramicroscopy 222 (2021) 113203

Contents lists available at ScienceDirect

Ultramicroscopy

journal homepage: www.elsevier.com/locate/ultramic

Adaptive domain misorientation approach for the EBSD measurement of deformation induced dislocation sub-structures

Pauli Lehto

Department of Mechanical Engineering, Aalto University, School of Engineering, P.O. BOX 14100, FIN-00076 Aalto, Finland

ARTICLE INFO

Keywords:
Deformation pattern
Polycrystalline material
Sub-grain
Dislocation cell
Lattice curvature
Kernel average misorientation (KAM)

ABSTRACT

In the current work a novel domain misorientation approach is introduced, which can resolve sub-grains and dislocation cells using conventional EBSD. The measurement principle utilises measurement domains that are grown radially until a specified misorientation value has been reached. This enables stochastic analysis of local misorientation to be carried out within individual sub-grains and dislocation cells. The sub-structural boundaries are classified according to the total misorientation across the boundary region, the thickness of which can vary from approximately one hundred nanometres to several hundred nanometres. Sub-grain boundaries with a total misorientation larger than 2° are resolved effectively for as-measured Hough-based EBSD data. De-noising of the EBSD data allows small dislocation cells to be resolved, typically having a misorientation of 0.4° – 1.0°. The developed approach is applied to various deformed metals, showing a significant increase in the level of detail resolved compared to the conventional kernel misorientation approach. The developed adaptive domain misorientation approach and the EBSD datasets measured for this publication are provided as open access.

1. Introduction

Measurement of plastic deformation and the microstructural changes are fundamental to understanding the material damage mechanisms. The study of deformation mechanisms spans over several length scales from the macroscopic response to the motion of individual dislocations. While a deformation state may appear uniform macroscopically, complex heterogenous deformation patterns develop in the microstructural length scale [1]. A significant body of research has been carried out to understand the nature and origins of the deformation heterogeneities. Research for polycrystalline materials has shown that as strain gradients are accommodated through lattice curvature, enabled by geometrically necessary dislocations (GNDs), heterogeneous intragranular deformation patterns are generated to achieve compatibility and an equilibrium energy state; see [1–7].

The source of heterogeneities are interfaces such as grain boundaries, which both restrict the rotation of the crystal lattice and inhibit the motion of dislocations [1,8]. The pile-up of dislocations at grain boundaries, as theorised by the Eshelby-Frank-Nabarro dislocation pile-up model [9], is a fundamental strengthening mechanism for many engineering materials. The grain boundary strengthening established by Hall [10] and Petch [11], known as the as the Hall-Petch relationship, predicts an increase in material strength with the inverse square root of the grain size. This relationship has been shown applicable to a large variety of materials and material properties [12]. Further insight to the mechanisms of grain boundary strengthening can be made by observing the evolution of the deformation patterns inside the grains. Muránsky et al. [13] showed that the accumulation of GNDs is a complex process with the GND density also increasing inside the grains, which leads to the formation of heterogeneous sub-structural deformation patterns. The study of deformation patterns in polycrystalline materials is made more complicated by the stochastic nature of the crystal structure, i.e. the spread of grain size and orientation, as they affect the activation of slip systems and compatibility of neighbouring grains for deformation [13].

The deformation patterns in polycrystals are material dependent, affected e.g. by the structure of the crystal lattice, chemical composition, magnitude of strain, strain rate and temperature [14,15]. For face-centred cubic (FCC) materials the plastic strain is accommodated in the microstructure by phase transformation, twinning, or formation of a dislocation cell structure depending on the stacking fault energy [15,16]. The cell-forming mechanism is commonly observed in many materials with different crystal structures, for example in copper (FCC) [17], aluminium (FCC) [18], magnesium alloys (HCP) [19] and iron (BCC and FCC) [14,20]. During the cell-forming process the lattice dislocations re-arrange to minimize the total energy state, forming dense

E-mail address: pauli.lehto@aalto.fi.

https://doi.org/10.1016/j.ultramic.2021.113203
Received 17 July 2020; Received in revised form 11 December 2020; Accepted 5 January 2021
Available online 20 January 2021

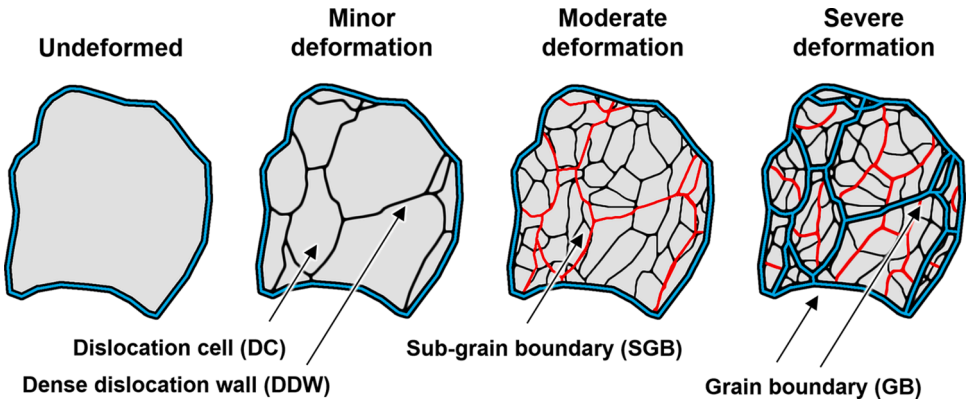

Figure 1. Schematic representation showing the evolution of a grain's sub-structure for a cell-forming material during plastic deformation, showing the formation of dislocation cells, sub-grains and ultimately new grain boundaries.

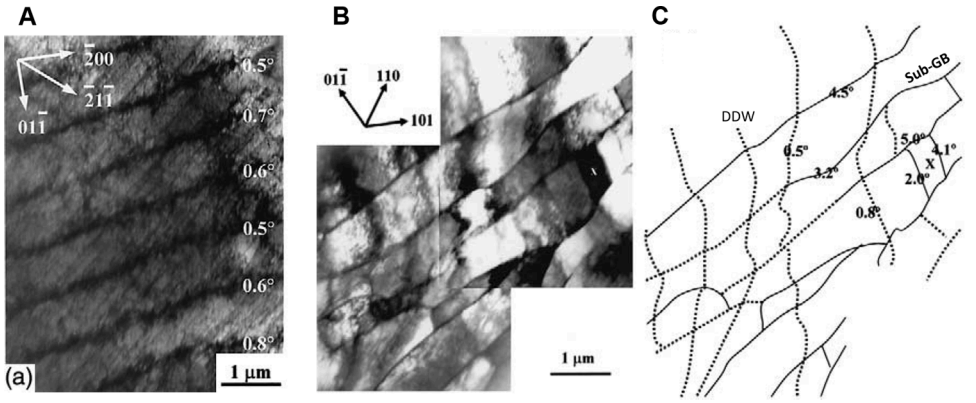

Figure 2. TEM images showing the appearance and misorientation of A) Dense dislocation walls, and B) Dense dislocation walls, dislocation cells and sub-grain boundaries for nanocrystalline pure Fe. C) Schematic representation of the sub-structure shown in B, including misorientation across selected DDWs (dashed) and sub-grain boundaries (solid). Reprinted from Tao et al. [14], with permission from Elsevier. Annotations (DDW, Sub-GB) have been added to sub-figure C by the author of this publication.

dislocation walls (DDWs) and dislocation tangles (DTs) inside the grains [14]. This creates dislocation cells that are confined by low angle boundaries (<1°) [14]; see Figure 1. Size of the dislocation cells ranges from several micrometres to the sub-micrometre regime, with size being proportional to the applied stress or strain [21,22]. With continued deformation, further re-arrangement and annihilation of the dislocations occurs, creating sub-grain boundaries with a higher misorientation angle compared to the DDWs [14]. Further deformation is enabled by the formation of new high-angle grain boundaries, and repetition of the refinement process inside the new grains. However, the sub-grain size will stop to refine as dislocation annihilation rate equals the dislocation multiplication rate [14]. This level of extreme grain refinement can be achieved for example with a severe plastic deformation process [23]. Deformation under elevated temperatures also increases the mobility of dislocations, promoting the formation of new grains [19].

The characteristics of the original grain boundaries and deformation induced sub-structural boundaries can be studied using transmission electron microscopy (TEM). Typically high angle boundaries (>10°) are considered as grain boundaries, with the transition across grains taking place within a few nanometres [24]. This definition is based on the simplification that most high angle boundaries are effective barriers for dislocation motion, however, misorientation angle alone does not accurately represent the deformation compatibility of two neighbouring grains [25–27]. For sub-structural boundaries the misorientation is considerably smaller, and the thickness of the boundaries can increase. Based on the TEM imaging of Tao et al. [14], shown in Figure 2, the sub-grain boundaries in iron can have a physical thickness of approximately 50 nm and the DDWs between 100 – 300 nm. Furthermore, the total misorientation across sub-grain boundaries is typically 2 – 5° and only 0.5 – 0.8° for DDWs [14]. As curvature of the crystal lattice is continuous [8], the orientation gradients typically extend beyond the physical thickness of the sub-structural boundaries. A considerable increase in the lattice curvature is typically observed at the boundary region [28]. Thus, in order to effectively measure the deformation patterns, the analysis procedure should consider the cell-forming deformation process and be able to detect the locations of increased lattice curvature. The implications of spatial and angular resolution limitations must be considered in order to effectively carry out the analyses.

Because TEM is limited to a small area of observation and is thus time-consuming, material deformation is commonly measured using scanning electron microscopy (SEM). Electron backscatter diffraction (EBSD) in a SEM is able to map large areas with good spatial resolution in a relatively short time [29], and it is the preferred engineering tool for deformation analysis. EBSD analysis resolves the crystal orientation by detecting lattice planes from a diffraction pattern using a Hough transformation process. The traditional Hough-based EBSD typically has an angular resolution of approximately 0.5° for misorientation and 2° for orientation [30]. The analysis of orientation data provided by EBSD enables plastic deformation to be quantified [31]. The level of deformation can be estimated with misorientation analysis, where the orientation of two or more data points is compared for individual grains or within calculational domains. The accuracy of the grain based analysis is dependent on an appropriate definition of the reference orientation, which is challenging for deformed polycrystalline materials [32].

To avoid the challenges of grain detection [33] and the proper selection of reference orientation, the kernel average misorientation (KAM) is often used as a qualitative measure of plastic deformation localisation. The kernel misorientation measures the average misorientation between a central point and its nearest neighbours [34]. KAM has

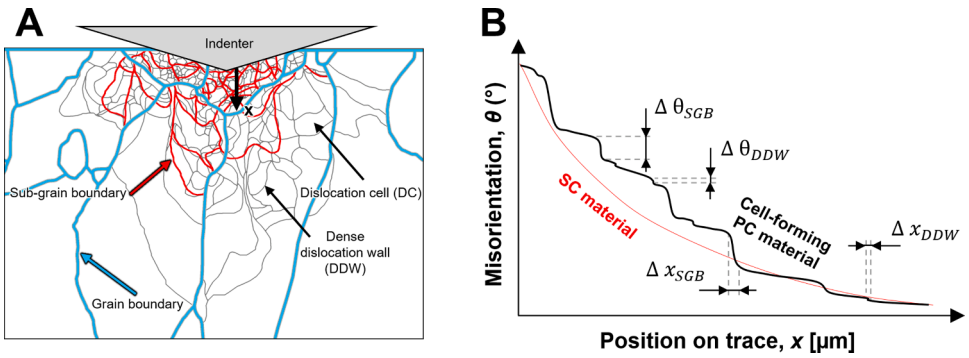

Figure 3. A) Generation of grain sub-structures in a polycrystalline material under a local strain gradient imposed by a hardness indenter. B) Schematic presentation of lattice curvature measured as misorientation along the trace shown in A by the letter x. The misorientation gradient for single crystalline copper is extracted from the work of Kiener et al. [47] and schematised to highlight the differences between single crystalline (SC) and cell-forming polycrystalline (PC) materials.

been shown to be dependent on the GND density [34], i.e. lattice curvature, and to correspond to the applied macroscopic strain when averaged over multiple grains or entire measurement fields [32,34,35]. The size of the kernel is defined as the number of nearest neighbours from a central point, with analysis typically carried out using 1 – 3 nearest neighbours [31]. The results obtained with KAM are sensitive to several factors [31]: 1) angular and spatial resolution of data, 2) size of the kernel, 3) the threshold angle θ_{max} for excluding data-points originating from neighbouring grains, usually in the range 2 – 5°. In particular, the analysis of misorientation angles smaller than 0.5° is restricted by the angular resolution of EBSD. Thus, general trends and locations of increased strains can be detected on a global scale, as demonstrated e.g. by Rollet et al. [36]. However, when accumulation and localisation of strain was evident, it was not possible to resolve clear sub-structures. Consequently, the conventional kernel misorientation approach is not well suited to the characterisation of sub-structures, as the shallow misorientation gradients across e.g. the DDWs are masked by the measurement noise of Hough-based EBSD. While the quality of classical EBSD-based analyses can be improved with various noise reduction strategies [37–41], the characterisation of DDWs remains a challenge due to the interplay of EBSD's spatial and angular resolution with the thickness and misorientation of DDWs, as well as with the size of dislocation cells. Thus, the EBSD-based analysis methods need to be developed beyond the nearest-neighbour or point-to-point analysis procedures, as proposed in this study, in order to detect the small local misorientation gradients at the DDWs.

This work presents a novel domain misorientation approach for the measurement of deformation induced dislocation sub-structures. The size of the measurement domain is defined based on material deformation mechanisms. Thus, contrary to the conventional approach of a fixed 1 – 3 nearest neighbour kernel, the size of the measurement domain is adapted to the physical size of the sub-structures. The measurement approach is based on statistical analysis of the measurement domain to detect the locations where the misorientation gradient changes. This shifts the measurement strategy from trying to capture the gradual change in orientation at the sub-GBs and DDWs to an approach where the misorientation of the boundaries is measured in relation to the neighbouring sub-structural units. This makes it possible to capture gradual low-angle boundaries that have a finite thickness larger than the spatial resolution of the data. It will be shown that the developed approach increases the signal-to-noise ratio of the measurement, making it possible to capture the sub-grain boundaries from as-measured Hough-based EBSD data. Furthermore, the efficacy of orientation data de-noising is demonstrated, enabling a well-defined dislocation cell structure to be resolved for the tested steel material. The developed methodology and the used EBSD datasets are provided as open access.

The paper is structured as follows. The adaptive domain misorientation approach is presented in the second section. The third section presents the details of EBSD measurements used for the validation of the developed methodology. The fourth section with the analysis results is divided into five subsections: the first and second subsections are dedicated to resolving the heterogeneous deformation patterns, including the sub-grain boundaries and the dislocation cell structure. A sensitivity analysis is carried out in the third subsection to demonstrate how measurement parameters, angular measurement noise and spatial resolution affect the measurements. In the fourth subsection the developed methodology is applied to open access EBSD datasets to demonstrate that deformation patterns can be resolved for various deformed metals with different processing histories. In the fifth sub-section the adaptive domain misorientation approach is compared to other SEM analysis methods. Finally, the results are discussed and reflected to the state of the art, and conclusions presented.

2. Adaptive domain misorientation approach

2.1. Deformation domain based misorientation analysis

Here we propose the methodology that can reveal the deformation induced dislocation sub-structures in polycrystalline materials. In order to develop EBSD-based analysis beyond the nearest-neighbour procedures, the measurement principle must consider the deformation mechanisms of the material. Thus, the proposed methodology considers the cell-forming deformation process [14], and accommodation of strain gradients through lattice curvature. The orientation gradients caused by lattice curvature can be measured using EBSD [34]. Two orientations are compared by defining the rotation angle-axis -pair that brings the two orientations into co-alignment [42]. Because multiple rotations achieve the co-alignment, the common convention is to use the one with the smallest rotation angle, termed as misorientation [42]. While accurate measurement of misorientation and especially the misorientation gradient are sensitive to angular measurement noise and the used spatial resolution, the total change in misorientation across the sub-structural boundaries is typically large enough to be measured. In order to capture the total change in misorientation, the measurement principle must be able to adapt the sampling area to the thickness of the boundary region containing the misorientation gradient. As deformation progresses, the misorientation across a specific sub-structural boundary will increase [43,44]. Thus, the initial dislocation cell structure created by the low-angle DDWs will evolve into sub-grain boundaries and eventually into new high angle grain boundaries, as shown schematically in Figure 1.

The deformation induced dislocation sub-structures are shown schematically for localised plastic deformation in Figure 3A. A hardness indentation is used as an example, because it naturally includes a local deformation gradient and thus, the dislocation sub-structures vary as a function of distance to the indented surface. The grains under the

relatively large indentations are expected to be highly deformed, consisting of a mixture of sub-grains and fine dislocation cells. The density of sub-structural boundaries decreases as a function of distance, with large dislocation cells and individual DDWs observed at the edges of the deformed material volume. The expected misorientation profile under a hardness indentation is defined in Figure 3B. The maximum misorientation near the indenter is defined by the geometry of the indenter, being 22° for sufficiently large Vickers indentations in single crystalline (SC) materials [45]. The same observation can also be made for polycrystalline (PC) materials [46]. While for SC materials the misorientation gradient is continuous and smooth [47], cell-forming PC materials have significant variations in the misorientation gradient; see Figure 3B. These variations are a result of dislocations re-arranging into energetically favourable configurations [14], i.e. the formation of the sub-structural boundaries. Thus, the sub-structures can be captured for cell-forming PC materials by measuring the changes in the misorientation gradient.

The classification of the misorientation gradients is carried out with two parameters in the current study: the total misorientation across the boundary region, denoted $\Delta\theta$, and the thickness of the boundary region Δx, defined as the region with a high misorientation gradient relative to its surroundings. In order to track the evolution of plastic deformation, the sub-structures are categorized into dense dislocation walls ($\Delta\theta_{DDW}$) and sub-grain boundaries ($\Delta\theta_{SGB}$) according to the total misorientation. The values used in this study are based on the direct TEM measurements of Tao et al. on BCC iron [14], with the (minimum) misorientation across dense dislocation walls defined as $\Delta\theta_{DDW}$=0.5°, and across sub-grain boundaries as $\Delta\theta_{SGB}$=2.0°; see Figure 3B. The difficulty in measuring the sub-structural boundaries is that the thickness of the boundary region is unknown prior to the measurement. Furthermore, the thickness of the boundary region can be different for DDWs (Δx_{DDW}) and sub-grain boundaries (Δx_{SGB}), and vary from boundary to boundary; see Figure 3B. To solve this problem in the domain misorientation approach, the size of the measurement area is not pre-defined but determined adaptively such that the measurement area is grown radially until the specified misorientation value, e.g. $\Delta\theta_{DDW}$=0.5°, has been reached.

2.2. Sampling approach

The sampling approach in this study can be considered as an evolution of the conventional kernel misorientation approach. The differentiating factor is that the pre-defined (maximum) size of the kernel is significantly larger, corresponding up to 100 nearest neighbours, which is physically 20.1×20.1 μm and 201×201 μm at step sizes of 0.1 μm and 1 μm, respectively. In general, it can be assumed that the required kernel size is larger than the average grain size in order to capture the grain sub-division process. A procedure for the iterative definition of required kernel size is presented in Appendix C. For further reference, the term 'kernel size' refers to the maximum square kernel size set by the operator.

The measurement area is defined based on the above-mentioned boundary region misorientations $\Delta\theta$, such that the measurement area is grown radially inside the kernel until the pre-defined misorientation value is exceeded. The measurement area is expected to be continuous due to continuity of lattice curvature inside a single grain [8,28], and thus only the interconnected central region is considered for the measurement. Similarly, measurements originating from neighbouring grains are excluded. The aim of this approach is to restrict the measurement area to the interior of sub-structural units, and to capture the complete misorientation gradient at e.g. the DDWs to maximize the signal to noise ratio. The misorientation axis is neglected in the determination of the measurement area, as it is very sensitive to measurement noise for small misorientations in EBSD analysis [48]. Thus, in the proposed approach the measurement area within the misorientation angle $\Delta\theta$ is determined first, and then the rotation directions are analysed within that area.

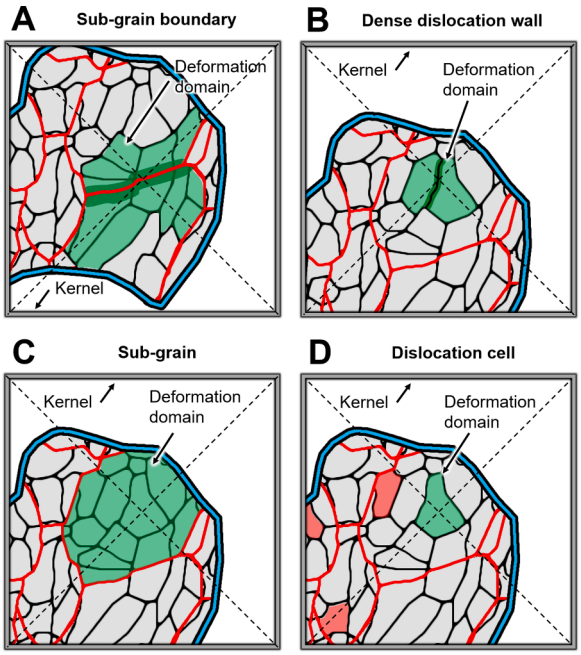

Figure 4. Schematic illustration of deformation domain size for A) sub-grain boundaries ($\Delta\theta_{SGB}$=2°), B) dense dislocation walls ($\Delta\theta_{DDW}$=0.5°), C) Sub-grains ($\Delta\theta_{SGB}$=2°) and D) dislocation cells ($\Delta\theta_{DDW}$=0.5°). The shaded green area is the deformation domain within the misorientation value, and red shading is an excluded area.

Schematic examples of expected shape and size of the measurement areas are shown in Figure 4 for the sub-structural units. Figure 4A shows the sub-grain boundary (SGB), with the kernel shown by the large grey square. Depending on the misorientation of the specific sub-grain boundary, the effective measurement area can only sample the vicinity of the sub-grain boundary (dark green), or multiple dislocation cells adjacent to the sub-grain boundary (light green). The effective measurement area is termed as the 'deformation domain' for further reference. For convenience its size is converted to an equivalent area square, so it can be presented in the same units as the 'kernel size' set by the operator. Similarly, the deformation domain for DDWs in Figure 4B can sample only the vicinity of the DDW or the two neighbouring DCs depending on the misorientation profile. Depending on the spatial alignment of the measurement grid and the global misorientation gradient, the misorientation profile across a DDW can be asymmetric. This can create a situation where the deformation domain samples one dislocation cell entirely, but only extends to a portion of the other dislocation cell. For sub-grain and dislocation cell interiors the deformation domain is expected to cover the entire interior, as shown in Figure 4C and Figure 4D. It is noted that the total misorientation inside large sub-grains can exceed the misorientation value $\Delta\theta_{SGB}$ despite a shallower gradient, thus reducing the size of the deformation domain. It will be shown next that the average misorientation of the deformation domain is a proxy to the misorientation gradient, and that it is less sensitive to measurement noise than the conventional approaches.

2.3. Misorientation analysis for the deformation domain

The benefit of the adaptive domain misorientation approach is that it enables stochastic misorientation analysis both inside the sub-structural domains and on the sub-structural boundaries. A schematic representation of the distributions measured with the domain misorientation approach is shown in Figure 5A. A narrow distribution of small misorientation values is expected for the undeformed material, as shown by (1). As deformation takes place the dislocation density increases, leading to larger misorientations within the dislocation cells (2). As

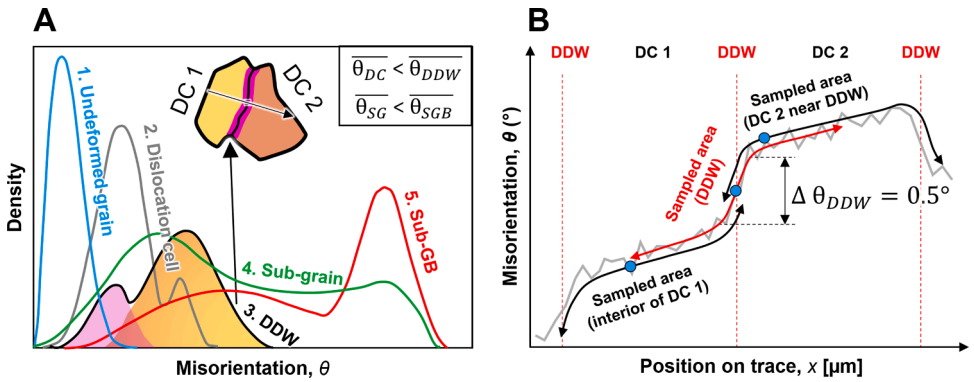

Figure 5. A) Schematic representation of misorientation histograms for different sub-structural features. B) Misorientation line-trace shown in the inset of (A), where the black and red arrowed splines show the deformation domain at three different measurement points for the criterion $\Delta\theta_{DDW}=0.5°$.

shown in Figure 5B, the misorientation gradient inside DCs is shallow, and thus most sampled orientations are in near-similar orientation. A bi-modal distribution is produced for the DCs by sampling of the steeper misorientation gradient at the DDW. At the DDWs (3.) fewer neighbouring points are in near similar orientation, with misorientation quickly increasing as a function of distance due to the large misorientation gradient. For this reason, the proportions of the bi-modal distributions change, as shown schematically in Figure 5A. Thus, the average misorientation of the deformation domain is significantly larger for DDWs ($\overline{\theta_{DDW}}$) compared to DCs ($\overline{\theta_{DC}}$), and can be used as a proxy for detecting areas with high misorientation gradients. Sampling of a larger area also increases the signal-to-noise ratio, as misorientation typically increases as a function of distance [35]. Here it should be noted that usually the misorientation profiles are monotonically increasing or decreasing between adjacent dislocation cells due to the global misorientation gradient. In the rare case that neighbouring DDW's share the same misorientation axis and opposite rotation directions, the total misorientation $\Delta\theta_{DDW}$ is still usually able to restrict the measurement area to the interior region.

Similar principles apply to the measurement of sub-grains. Sub-grain interiors are assumed to include multiple DCs, and thus a broad dispersion of misorientations is expected, as shown by (4.) in Figure 5A. The assumption of a large misorientation gradient applies for the sub-grain boundary (5.) as well, with the highest peak of the bi-modal distribution expected to shift from low-moderate misorientations to high misorientations. The median value is used to better differentiate these broad dispersions, as it captures the change of skewness from positive to negative. This will increase the contrast of the sub-grain boundaries, and therefore the term Domain Median Misorientation (DMM) is introduced in addition to the Domain Average Misorientation (DAM). For clarity, the results obtained with the developed approach are referred to using terminology 'adaptive DAM' and 'adaptive DMM' in order to differentiate from the 'conventional KAM'. The boundary region misorientation used in the analyses will be explicitly mentioned with each measurement result, e.g. adaptive DAM ($\Delta\theta_{DDW}=0.5°$) or adaptive DMM ($\Delta\theta_{SGB}=2°$).

3. Experimental data for approach verification

Experiments for various polycrystalline metals are utilised to show that the deformation induced sub-structures can be measured by the developed adaptive domain misorientation approach (i.e. DAM, DMM). Local plastic deformation experiments are carried out for verification of structural steel's deformation process, while existing literature EBSD datasets are used to investigate the method's sensitivity to material microstructure and material dependent deformation mechanisms.

3.1. Experiments for structural steel

A structural steel with a nominal yield strength of 355 MPa was used for the experimental verification. The characteristic properties of the material are shown in Table 1. The 6 mm thick steel plate is delivered in the normalised condition with a ferritic-pearlitic microstructure, composing of 78.6 ± 5.3% of primary ferrite and 21.4 ± 5.3% of pearlite [49]. The material has an average grain size of 10.0 µm, and a volume-weighted average grain size of 15.3 µm [49]. Grain size analysis was carried out with the methods published in [49,50], available as open source in Ref. [51].

To characterise the plastic deformation process of the steel, instrumented indentation testing was carried out. Prior to indentation experiments, the material section was mounted in an electrically conductive resin and grinded using P180-P4000 grit abrasive papers, followed by polishing with 3-µm and 1-µm diamond paste. Fine-polishing was carried out with 0.25-µm diamond paste, followed by colloidal silica polishing in a vibratory polisher to minimise the deformation induced by the sample preparation. A CSM Instruments instrumented indenter was used, utilising the micro-indentation tester with a four-sided Vickers pyramid tip. The test force was chosen at HV0.05 (490.5 mN), resulting in an average indentation depth of 3.3 µm and indentation diagonal of 23 µm. This size was found to be large enough for the plastic deformation zone to cover multiple grains. Linear 30 second load ramps were used with a 10 second pause time at peak load.

For analysis of the material microstructure and plastic deformation, hardness indentations were cross sectioned for scanning electron microscopy. The indentations are named for further reference as indentation 1 and indentation 2, see Figure 6A&B for location of the cross-sections. A custom serial sectioning approach was used, in which an indentation matrix is implemented to act as a depth gauge for material removal, and a 50µm thick electroless nickel plating [52] is deposited to protect the indentations. Long polishing times were used to minimise deformation on sample surfaces: 10 minutes for 3µm and 1µm diamond polishing, 12 minutes for 0.25 µm diamond polishing, and 10-24 hours

Table 1
Mechanical properties and chemical composition of the tested plate.

		Mechanical properties			Chemical composition											
Specimen	Grade	$R_{p0.2}$ (MPa)	R_m (MPa)	A (%)	C (wt. %)	Mn	P	S	Si	Al	Cu	Ni	Cr	V	Mo	Fe
BM.1	GL D36	343	472	34	0.11	0.96	0.021	0.007	0.25	0.043	0.03	0.03	0.02	0.002	0.002	Bal.

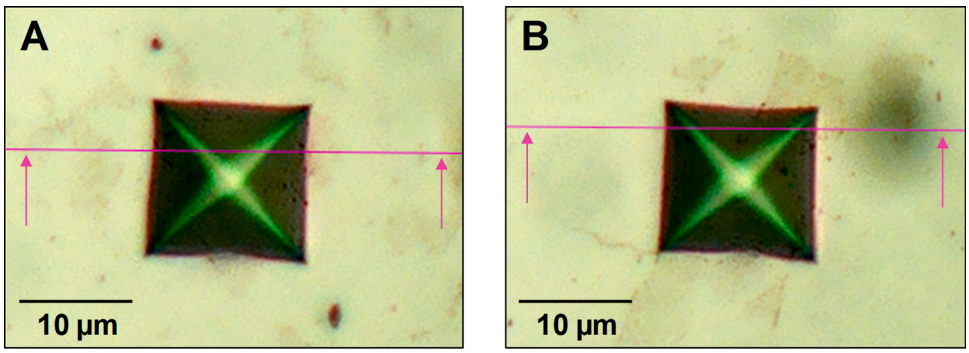

Figure 6. Location of the HV0.05 structural steel cross-sections for A) Indentation 1, and B) Indentation 2.

Table 2
Parameters used for EBSD data de-noising with the half-quadratic filtering in MTEX version 5.3.

Parameter	Value	Explanation
F.alpha	1	Regularization parameter, typical value 1
F.l1DataFit	TRUE	Use l ^1 norm for data fitting
F.l1TV	TRUE	Use l ^1 norm for regularization
F.iterMax	5000	Maximum number of iterations
F.tol	0.02°	Stopping criterium for the gradient descent
F.eps	1.E-03	l ^1 relaxation parameter
F.threshold	5°	Threshold for sub-grain boundaries (point-to-point)

for colloidal silica polishing depending on the specimen.

The samples were characterised using a Zeiss Ultra 55 field emission scanning electron microscope equipped with a Nordlys F+ camera. Channel 5 software from Oxford Instruments was used for the electron backscatter diffraction (EBSD) acquisition. The EBSD analyses were performed with a step size of 0.1 µm and 0.06 µm for Indentations 1 and 2, correspondingly. The acceleration voltage was 20 kV and the working distance approximately 19.5 mm. A 120 µm aperture was used in conjunction with 4×4 detector binning in order to shorten acquisition time of patterns and reduce drift during the measurement. Patterns were acquisitioned using an 8 ms exposure time, and the Hough resolution was set at 100. Number of bands for indexing was set from 5 to 8, with 8 being indexed for the entire acquisition areas. The measurement noise of the EBSD datasets was estimated using the methodology proposed by Kamaya [35], implemented using MTEX and available at Ref. [53]. No pattern overlap is expected to happen at the used step sizes of 0.06 µm and 0.1 µm. In addition, the Bruker e-Flash HR EBSD –detector, mounted in a Merlin VP Compact SEM, was used to capture a forescatter detector image for Indentation 1, providing superior orientation contrast [54] compared to the Nordlys F+ camera.

The EBSD data was post-processed and analysed using the open source toolbox MTEX version 5.3 [55,56]. The toolbox was operated using Matlab version R2020a. The orientation data was post-processed with the half-quadratic filter developed by Bergmann et al. [38] to reduce measurement noise, and assign orientations to the non-indexed points. Contrary to other commonly used filters, half-quadratic

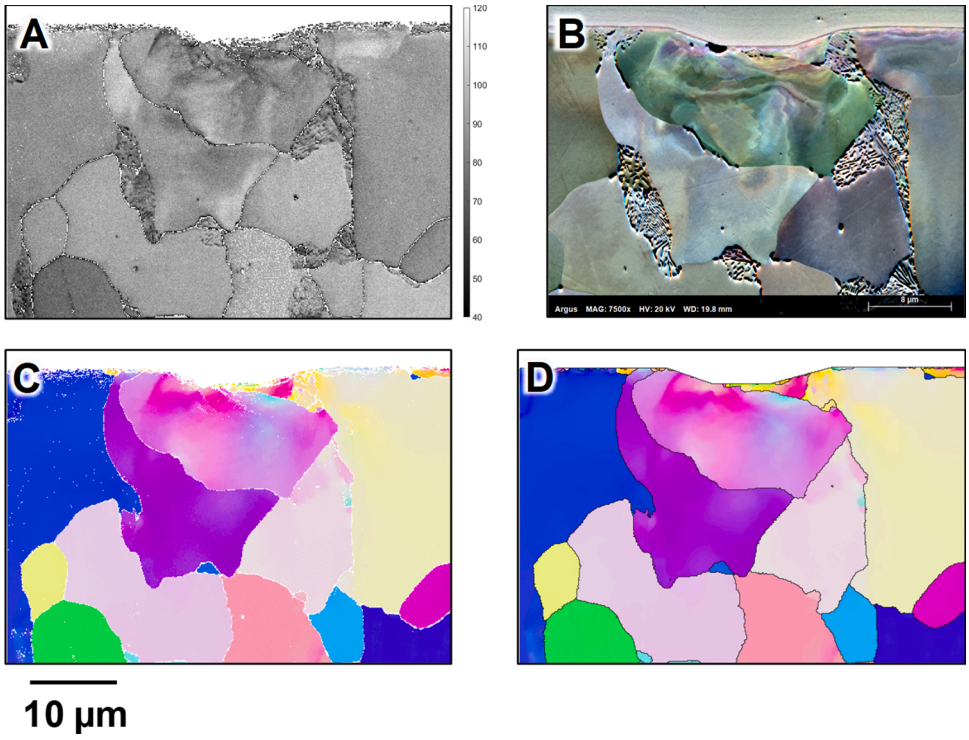

Figure 7. Base metal indentation 1 mapped at 0.1 µm step size, showing: A) Band contrast map, B) Forescatter detector image (FSD) showing orientation contrast and phase structure, C) Raw orientation map (IPF-X), D) Orientation map after de-noising and masking (IPF-X), with >10° grain boundaries superimposed. Orientation data is shown only for a cropped section of the dataset. Indexing rate of the entire map is 98% omitting the nickel-plated area.

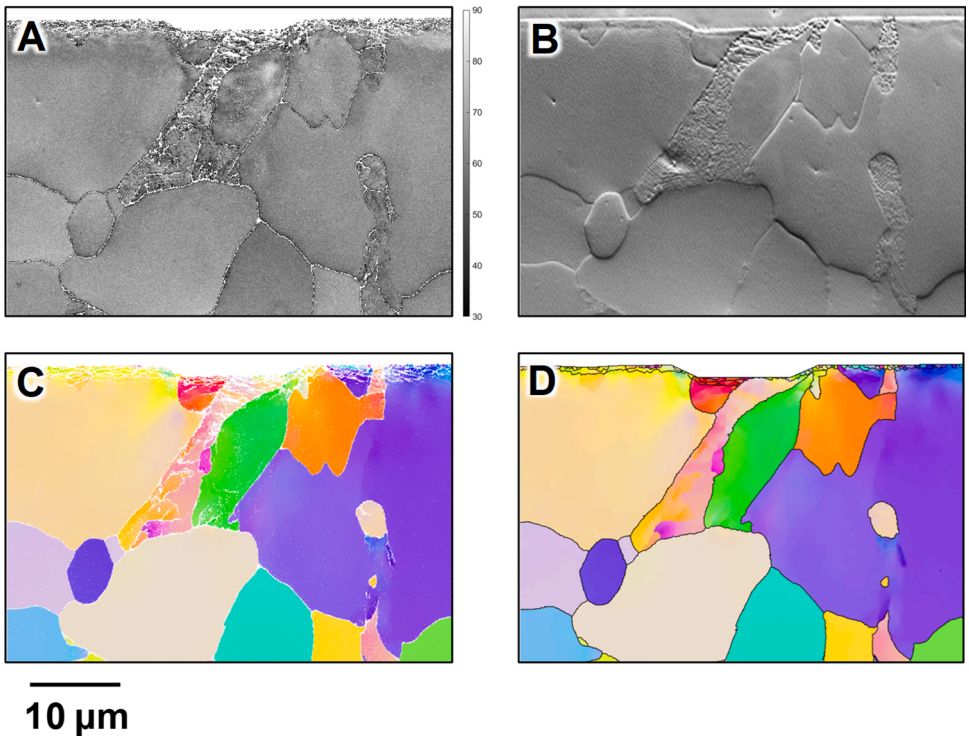

Figure 8. Base metal indentation 2 mapped at 0.06 µm step size, showing: A) Band contrast map, B) Forescatter detector image (FSD) showing orientation contrast and phase structure, C) Raw orientation map (IPF-X), D) Orientation map after de-noising and masking (IPF-X), with >10° grain boundaries superimposed. Orientation data is shown only for a cropped section of the dataset. Indexing rate of the entire map is 96% omitting the nickel-plated area.

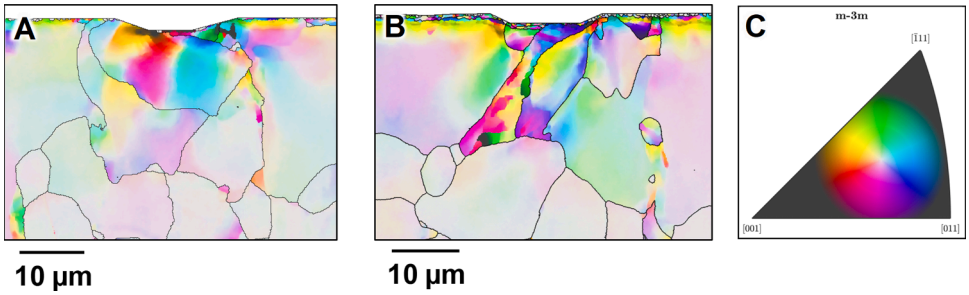

Figure 9. Grain-based orientation maps, where orientation is presented as a deviation from the grain's mean orientation for A) Indentation 1, B) Indentation 2. C) The colour key, extending 15° around the grain mean orientation. More saturated colours represent larger deviation from the mean orientation, with dark grey indicating more than 15°.

filtering is edge-preserving, and thus suitable for the analysis of sub--structural features. The implementation in MTEX version 5.3 is used, and it should be noted that its parameters differ from those in previous versions, e.g. 5.0.3. The used de-noising parameters are shown in Table 2. The EBSD datasets used in this publication are available as open access from Ref. [57].

Analysis of the orientation data is carried out with MTEX, including basic functionality to visualise orientation maps and grain boundaries. The conventional KAM used in this publication is defined as a 3×3 square kernel, with misorientations larger than $\theta_{max}=2^{\circ}$ excluded. The adaptive domain misorientation approach is also built upon the functionalities of MTEX. The analysis method is published as open source in Refs. [53,58].

The band contrast, forescatter detector and orientation maps for Indentations 1 and 2 are shown in Figure 7 and Figure 8, respectively. The indexing success rate is very good for both specimens (sub-figure C), with some second phase areas having lower indexing success for Indentation 2. Analysis will be focused on ferrite grains, so this will not hinder the analysis. The de-noised data (sub-figure D) shows minimal changes to orientation data, with the general outlook of the maps being identical. No new grain boundaries have been created by the local plastic deformation, making it easier to distinguish the original and deformation induced boundaries. As the deformation has caused rather smooth orientation gradients, no deformation patterns show up clearly inside the grains in the orientation maps (C-D), band contrast maps (A) or forescatter detector images (B). To better visualise the orientation gradients inside the deformed grains, a grain-based orientation map (Grain IPF) is shown in Figure 9. The orientation is presented relative to the mean orientation of each grain within a 15° range, with stronger colour saturation indicating larger misorientation. This reveals the deformed areas, and rotational patterns inside the grains. This analysis resolves sub-structural rotation patterns for the ferrite grains. The clearest sub-structural deformation pattern is visible for the second phase pearlite of Indentation 2, and it has been caused by the solidification process of the steel.

Table 3
Details and grain size measurement results for the open access EBSD datasets of A) deformed interstitial free steel [59], B) Ti-64 titanium alloy [60,61], C) AZ31 magnesium alloy strained to 2% [62,63], D) A690 nickel alloy strained to 2% [65,66].

Dataset	Step size	Map size	GBs	d	d_v	Indexing rate
IF steel	0.4 μm	410×547	>5°	16.2 μm	23.3 μm	92% Ferrite
TI-64 Alloy	0.15 μm	750×1000	>5°	3.95 μm	8.74 μm	95% Ti, 3.3% Ti-β
AZ31 Mg-alloy	0.23 μm	482×511	>10°	8.50 μm	14.5 μm	92% Mg
A690 Ni-alloy	0.71 μm	773×1535	>5°	12.9 μm	25.5 μm	100% Ni

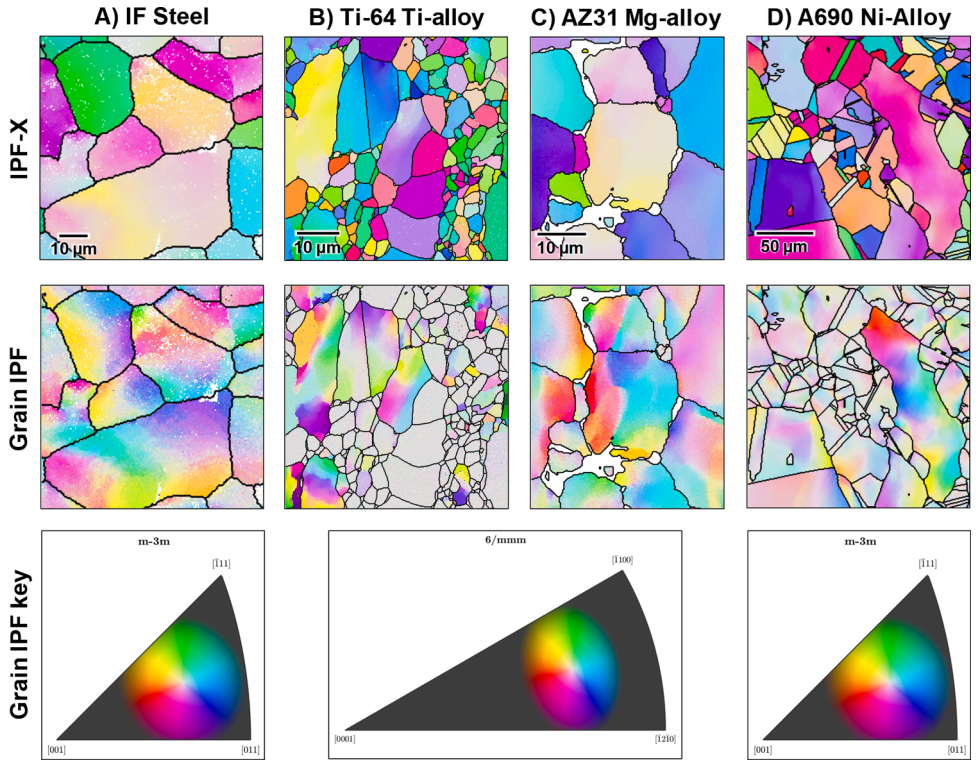

Figure 10. The orientation maps (IPF-X) and grain-based orientation maps are shown for open access EBSD datasets of A) deformed interstitial free steel [59], B) Ti-64 titanium alloy [60,61], C) AZ31 magnesium alloy strained to 2% [62,63], D) A690 nickel alloy strained to 2% [65,66]. Only a small section of the entire EBSD maps are shown. The colour keys extend 15° around the grain mean orientation, and the as-measured raw data is shown for all cases.

3.2. Literature EBSD datasets

To investigate the method's sensitivity to material microstructure and material dependent deformation mechanisms, several literature EBSD datasets are analysed; see Table 3 for details on the datasets. Only subsets of the data are displayed in this publication, with the analysis carried out for the entire datasets outside image borders. The orientation maps for the selected subsets are shown in Figure 10. The first dataset shown in (A) is a deformed interstitial free (IF) steel measured by Britton and Hickey [59]. This dataset is selected to study the deformation patterns of ferrite under uniaxial tension instead of indentation testing. The dataset has obvious orientation gradients caused by deformation, with sub-granular regions highlighted by the grain IPF. Second dataset shown in (B) is a Ti-64 titanium alloy subjected to unidirectional rolling measured by Britton et al. [60,61]. This sample has a combination of bi-modal grain size distribution and orientation gradients in some grains due to the rolling process, which can be challenging to assess using conventional methods.

The third dataset shown in (C) is an AZ31 Mg-alloy subjected to 2% strain, as measured by Orozco-Caballero and Quinta da Fonseca [62,63], with high resolution DIC data also available [64]. Blurred outlines of sub-granular boundaries have been resolved in the original publication for the central grain by a 3rd nearest neighbour analysis [63], also evident in the grain IPF. For this dataset the aim is to improve the visibility of the sub-grain boundaries, and to find out if finer sub-structures can be resolved. The fourth dataset shown in (D) is A690 Nickel-alloy subjected to 2% strain, as measured by Harte et al. [65,66], also including high resolution DIC data. The dataset has a remarkably low noise level, and orientation gradients especially in the elongated grain on the right side. Due to the high quality of the data, no post-processing will be applied for the analysis of this dataset. For other datasets, the de-noising parameters shown in Table 2 have been used prior to sub-structural analysis. In addition, the single pixel wild orientation spikes were removed prior to de-noising for the IF steel and Ti-64 titanium alloy. This is the recommended procedure by Hielscher et al. [40], as the half-quadratic filter is not able to differentiate impulsive noise from sub-grain boundaries defined by the parameter *F. threshold*. Next it will be shown that by using the adaptive domain misorientation approach, the deformation induced sub-structures can be measured for polycrystalline structural steel.

4. Results

4.1. Detection of sub-grain boundaries

The structural steel indentations are utilised for measuring the evolution of plasticity induced deformation patterns. First, emphasis is given to resolving the sub-structural boundaries that are typically

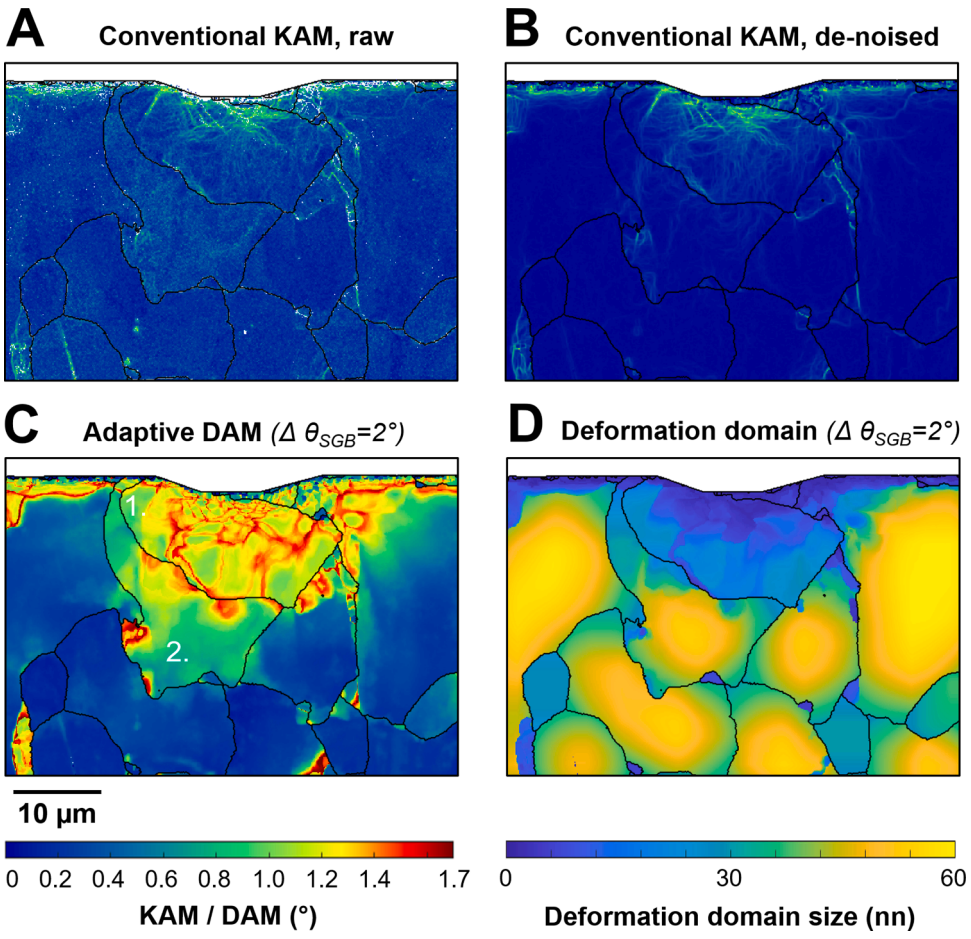

Figure 11. Conventional kernel average misorientation (1st nearest neighbours) calculated for the structural steel Indentation 1 using A) as-measured data and B) de-noised data. C) Sub-grain boundary analysis using the adaptive domain misorientation approach ($\Delta\theta_{SGB}=2^{\circ}$, kernel size 60 nn). Data extends beyond the shown region. D) Size of deformation domain, i.e. size of the sampling area for the analysis shown in C.

misoriented by more than 2°. The local misorientation measurements for structural steel Indentation 1 using conventional KAM and the adaptive DAM approaches are shown in Figure 11. The conventional KAM is sensitive to the measurement noise (Figure 11A), as the general noise level of Hough-based EBSD masks most of the details and makes it impossible to distinguish the extent of deformation accurately. As the de-noising approach is applied (Figure 11B), a large amount of details is revealed in the grain underneath the indenter. The measurement is influenced by the global orientation gradient of the indentation, resulting in larger misorientations near the surface. On the contrary, the adaptive DAM reveals a network of evenly misoriented boundaries (Figure 11C). The used kernel size of 60 nearest neighbours is large enough to sample neighbouring sub-grains, which is made evident by the reduced deformation domain sizes shown in Figure 11D. Continuity and consistency is observed in the deformation domain size, with clear sub-structural patterns also being resolved in the highly deformed grain, denoted (1) in Figure 11C. Elsewhere the deformation domain can reach the pre-set kernel size for the largest grains. Appropriate kernel size can be determined iteratively by increasing its size, with both the adaptive DAM and deformation domain size converging at sufficiently large kernel sizes; see Appendix C and Supplementary Video 1 for details on kernel size selection and convergence.

It is clear that the size of the sub-structural features resolved by adaptive DAM (Figure 11C) is significantly larger than those revealed by the conventional KAM (Figure 11B). This strongly indicates that by analysing a misorientation range defined by the value $\Delta\theta_{SGB}=2^{\circ}$, only a portion of the sub-structures are captured, likely representing the sub-grain boundaries. In addition to the sub-grain boundaries, significant differences are observed in the average level of deformation in different grains using the adaptive DAM. It clearly shows that there is significant deformation in the next grain as well, denoted (2) in Figure 11C. This is also visible as reduced deformation domain size in Figure 11D. Thus, the adaptive DAM also measures developing orientation gradients prior to the formation of the sub-grain boundaries.

While the deformation domain shows continuity in its size, the shape of the deformation domain is also fundamental to the sampling of the adaptive domain misorientation approach. Figure 12A-C illustrates the deformation domain's shape, indicated by the dashed black line, when the measurement point is traversed from the centre of a sub-grain towards a sub-grain boundary. In the centre of the sub-grain (Figure 12A), the deformation domain matches the sub-granular boundaries as intended in the measurement approach. When measurement is carried out near to the sub-grain boundary (Figure 12B), material is sampled from both sides of the boundary, leading to a slight increase in deformation domain size. When the measurement point is on the sub-grain boundary (Figure 12C), the deformation domain's shape remains similar with slight extension on the right side and reduction on the left side of the boundary. Thus, despite the measurement point having moved significantly, the area of sampled material has remained consistent. Therefore, analyses are carried out in the sub-granular level without accurately detecting the pixel-to-pixel boundary locations that is conventionally required in grain-based EBSD analyses.

To effectively visualise the sub-grain boundaries, the shape of the misorientation distribution needs to be considered. The distributions for the three measurement points are shown in Figure 12D-F. The multi-modal nature of the distributions is shown by the parametric fit,

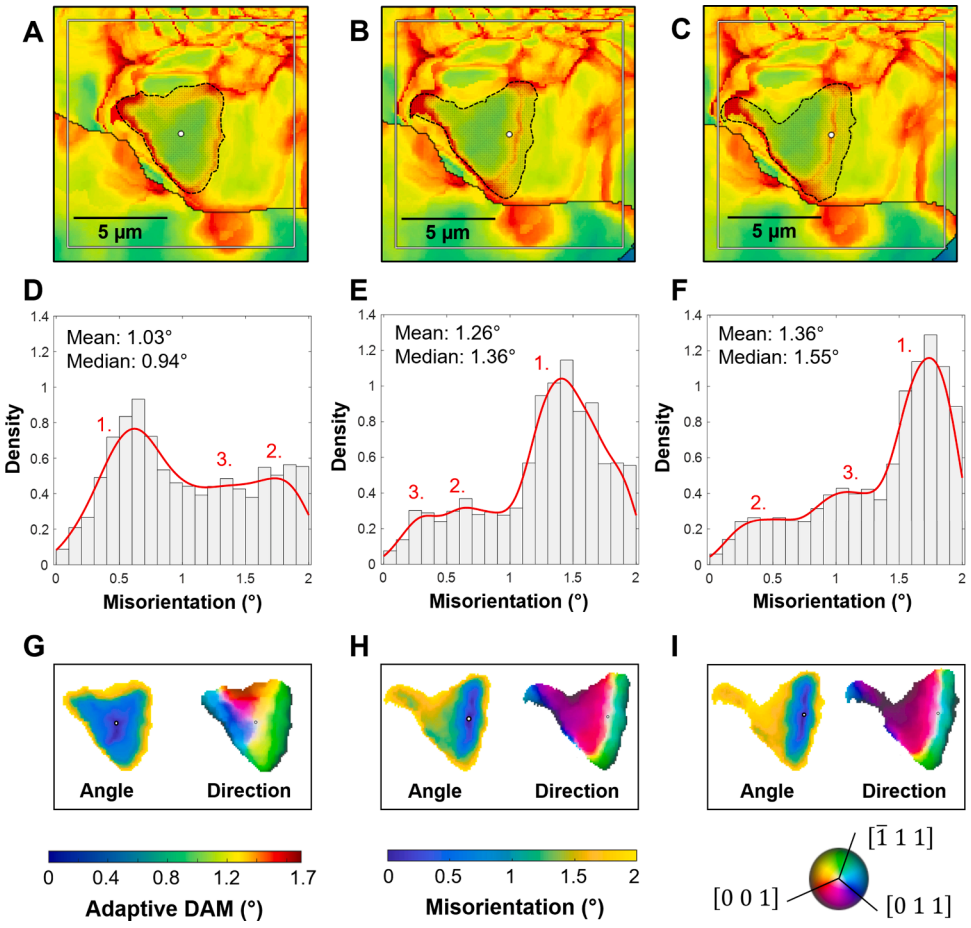

Figure 12. A-C) Adaptive DAM ($\Delta\theta_{SGB}$=2.0°) showing the deformation domain for different locations with the dashed black line. D-F) Corresponding misorientation histograms and parametric fits. The numbering of the peaks indicates the origin of the measurements: 1) Sub-grain interior, 2) Sub-grain boundary, 3) Region with gradual change in misorientation gradient near the sub-grain boundary. G-I) Misorientation angle and rotation direction for the deformation domains. The direction colour key represents a maximum misorientation of 2° from the reference point.

which could be further interpreted by dividing into three normal distributions. Physically these three distributions originate from areas with different misorientation gradients, numbered as: 1) the interior of the sub-grain, 2) the sub-grain boundary, and 3) near the sub-grain boundary where the misorientation gradient changes gradually. Inside the sub-grain (Figure 12D) the highest peak is at approximately 0.6° and has a long tail extending to 2°. The misorientation angle (Figure 12G) shows that the highest peak (1.) of small misorientations originates from inside the sub-grain, the tail (2.) originates from the sub-grain boundary and the tertiary peak near the sub-grain boundaries (3). The rotation direction (Figure 12G) shows multiple domains, indicating a dislocation cell structure inside the sub-grain. The same three sources of misorientation are visible in the other two measurements, however, their locations and proportions change. As the measurement point is close to the sub-grain boundary (Figure 12E), the highest misorientation peak (1.) shifts towards larger angles, still originating from the interior of the grain. As shown by the misorientation angle (Figure 12H), only a narrow band of the sampled material is in near-similar orientation (3.). The

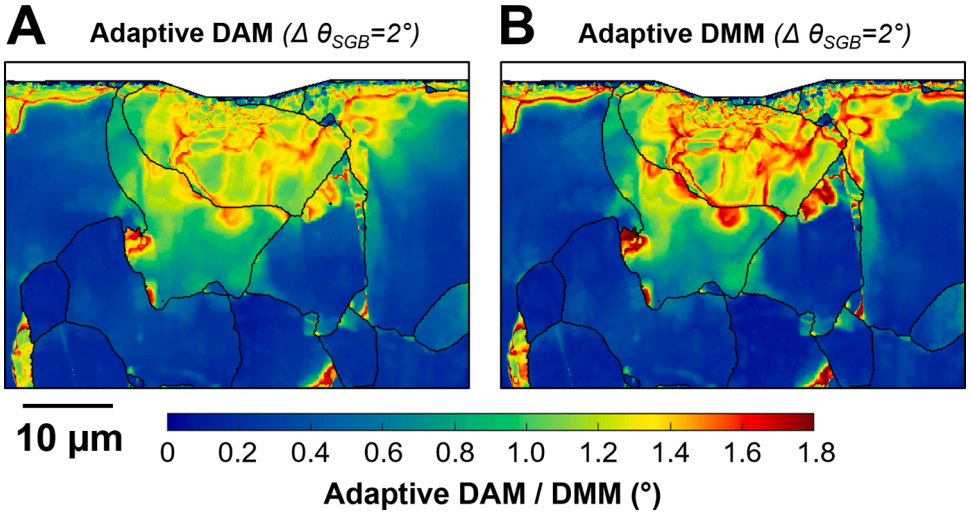

Figure 13. Adaptive domain misorientation defined as A) the average value (DAM) and B) the median value (DMM).

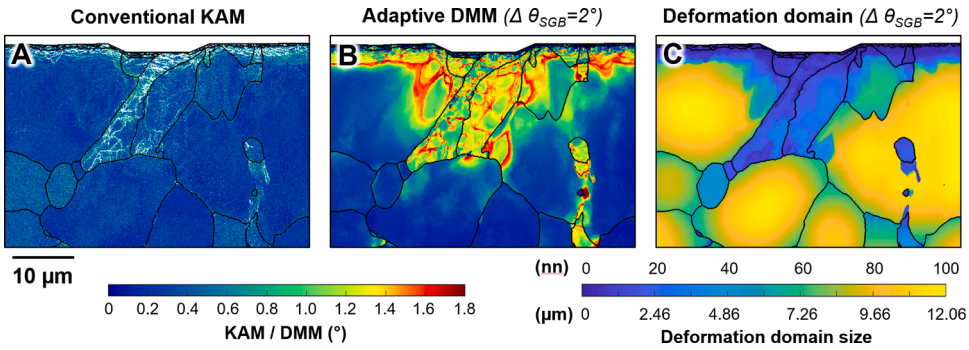

Figure 14. Structural steel indentation 2 mapped at a 0.06 µm step size, showing: A) Conventional KAM (1 nn) with the raw data. B) Adaptive DMM showing sub-grains (12.06×12.06 µm kernel size). C) Deformation domain size for the adaptive domain misorientation.

second highest peak (2.) originates from the sub-grain boundary, where rotation directions are consistent (Figure 12H). At the sub-grain boundary the highest peak (1.) shifts to larger misorientation values, originating mostly from the interior of the sub-grain on the left side (Figure 12I). The misorientation profile at the sub-grain boundary is symmetric, corresponding to the lowest peak (2.), also showing a consistent rotation direction along the sub-grain boundary (Figure 12I), similar to the near-boundary location in (Figure 12H). The second highest misorientation peak (3.) comes from the region where the misorientation changes gradually.

The source of the multi-modal distributions is the sampling of areas with different misorientation gradients. Depending on the location of the measurement point and the relationships of the misorientation gradients, the proportions of the distribution change. As a result of these changes, the average misorientation (DAM) provides contrast between the sub-structural regions. Because of the skewed shape of the distribution, the median values show better correspondence with the locations of the highest peaks. In comparison to the adaptive DAM (Figure 13A), the median value used in adaptive DMM (Figure 13B) increases the contrast of the sub-grain boundaries considerably. In addition, the contrast between deformed and non-deformed regions is improved elsewhere. For further analyses the adaptive DMM is used for resolving the sub-grain boundaries. As such, the numerical values of DAM and DMM do not directly reflect the misorientation of a specific boundary. Instead, they act as a proxy to the misorientation gradient, indicating the locations of sub-grain boundaries defined by the misorientation value $\Delta\theta_{SGB}$=2°. The average misorientation across the boundaries shown in Figure 13A is 2.1° (n=25), with the measurements varying between 1.0 – 4.1° when measured across the region with high adaptive DMM values. The thickness of the sub-grain boundary region (Δx_{SGB}) typically varies between 200 – 500 nm, sometimes being up to 800 – 900 nm.

4.2. Measurement of the dislocation cell structure

Evolution of plastic deformation can be tracked if the dislocation cell structure is differentiated from the sub-grain boundaries. However, the dislocation cells are more difficult to measure because they are bounded by dense dislocation walls, misoriented by approximately 0.5°. The dislocation cell structure is investigated for the structural steel Indentation 2 (see Figure 9B), which is mapped at a finer 0.06 µm step size to increase the spatial resolution for detection of the small dislocation cells. Using conventional KAM most deformation patterns are obscured by the measurement noise, with elevated levels near the indenter and in the second phase areas; see Figure 14A. By applying de-noising and the adaptive DMM presented in the previous section, the sub-granular boundaries and deformed grains are visualised in Figure 14B, similar to Indentation 1 used in the previous section. The deformation domain size in Figure 14C shows uniform large deformation domains elsewhere except in the heavily deformed area under the indenter.

Due to the smaller expected size of the deformation domains, the adaptive DAM (average misorientation) is better suited for the dislocation cell analysis. The misorientation value $\Delta\theta_{DDW}$=0.5° is utilised to reveal the small dislocation cells inside the sub-grains. To check that the size of the deformation domain is automatically limited to the dislocation cells, the kernel size is the same as used in the sub-grain analysis (12.06×12.06 µm, 100 nn). As shown in Figure 15A, a network of extremely fine dislocation cells is resolved in multiple grains. The second phase areas of pearlite also show deformation and fine substructures. The deformation domain size (Figure 15B) is considerably

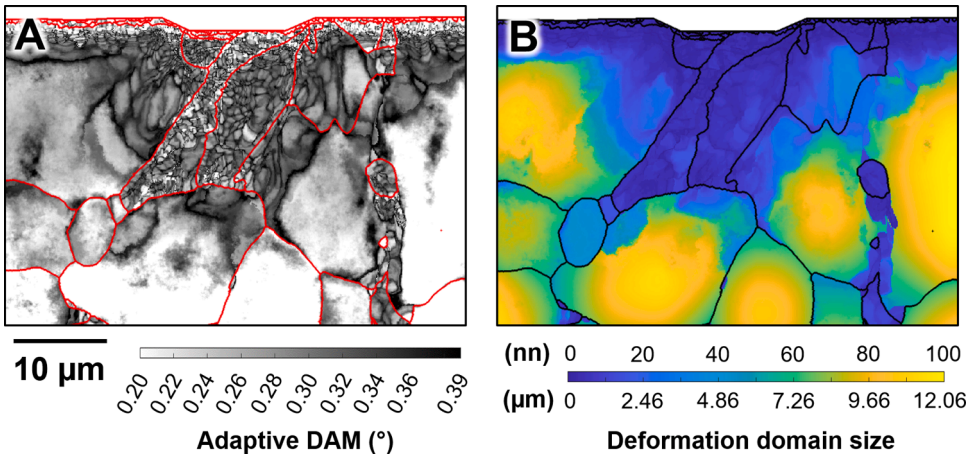

Figure 15. A) Adaptive domain misorientation showing dense dislocation walls and dislocation cells ($\Delta\theta_{DDW}$=0.5°, 12.06×12.06 µm kernel size). B) Deformation domain size for the measurement shown in (A).

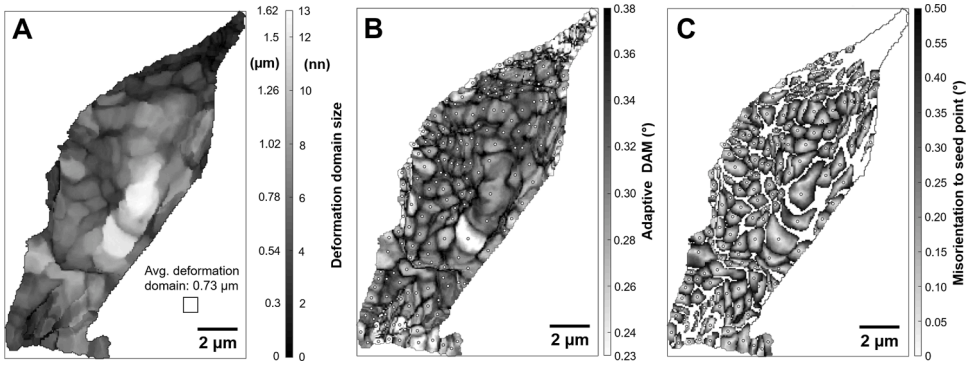

Figure 16. A) Enlargement of the heavily deformed grain for structural steel Indentation 2, showing the deformation domain size ($\Delta\theta_{DDW}$=0.5°). The inset shows the average square equivalent deformation domain size. B) Adaptive DAM ($\Delta\theta_{DDW}$=0.5°), with central points defined for most dislocation cells. C) Misorientation inside the dislocation cells relative to the central points, showing the deformation domains and orientation gradient for the selected points.

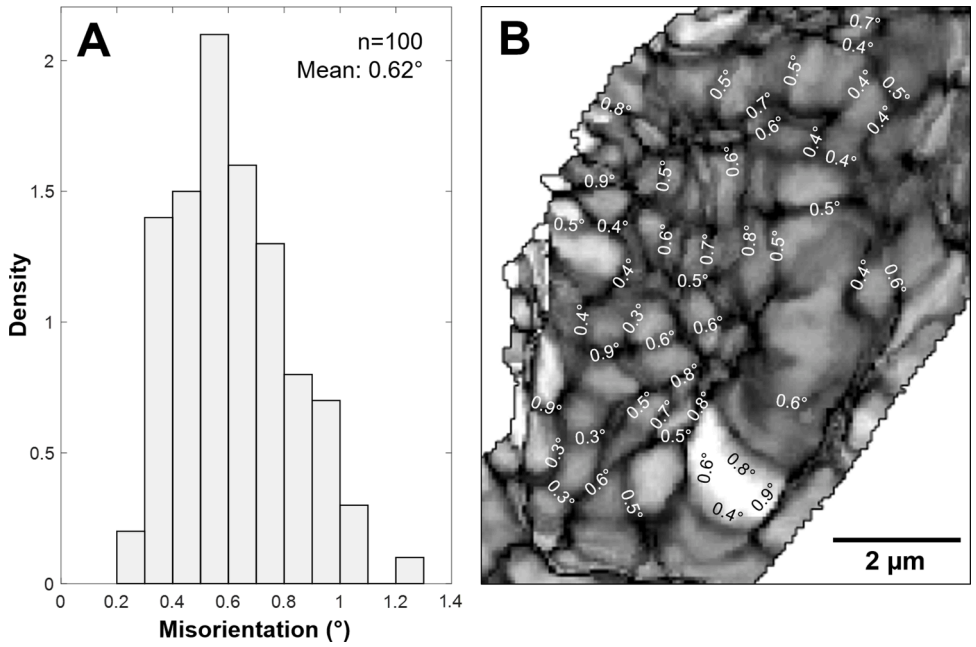

Figure 17. A) the histogram of all measured misorientations across the dense dislocation walls (n=100). The lower part of the grain has been excluded, as it's an area of secondary phase pearlite. B) Misorientation across selected dense dislocation walls (n=48) overlaid on adaptive DAM ($\Delta\theta_{DDW}$=0.5°).

smaller in many locations compared to the sub-grain analysis (Figure 14C), and the small deformation domains extend to regions where no sub-grains are observed. In the grains that are further away from the indenter, the deformation domain sizes are similar for both analyses. Reason for the similarity is the lack of sub-grains and dislocation cells that would limit the measurement area, and thus deformation domains are only limited by the grain boundaries. This also shows that the misorientation gradient is shallow inside the undeformed grains, as a misorientation gradient can also reduce the size of the deformation domain for large grains. These results indicate that the adaptive DAM works as intended such that the deformation domain adapts to the size of the dislocation cells.

To further understand how well the deformation domain adapts to the shape of the dislocation cells, more detailed analysis is carried out for an individual grain. The size of the deformation domain is shown with a restricted grayscale in Figure 16A for the highly deformed grain. The size of the deformation domain, i.e. sampling area at each point, reveals a well-defined network of dislocation cells. Consistent deformation domain size is observed inside individual dislocation cells, with reduced size observed on many dense dislocation walls compared to the neighbouring dislocation cells. Therefore, contrast is provided both by the size difference of neighbouring DCs, and the higher misorientation gradient of the DDWs.

The average deformation domain size shown in the inset of Figure 16A is comparable to the average size of the dislocation cells; see Appendix B for the dislocation cell size measurement. The deformation patterns are very similar to those shown by the average misorientation of each domain, i.e. the adaptive DAM shown in Figure 16B. To further show the misorientation gradient inside the DCs, the misorientation relative to the central points of the dislocation cells is shown in Figure 16C. Misorientation gradients are found to be quite shallow inside the DCs, with the high misorientation areas corresponding to the boundaries shown by the adaptive DAM (Figure 16B). Moreover, the shape of the deformation domains (Figure 16C) shows very good agreement with the dislocation cells (Figure 16B), confirming that misorientation analysis is being carried out inside individual dislocation cells.

While adaptive DAM measured with a misorientation value $\Delta\theta_{DDW}$=0.5° resolves the dislocation cells, it is expected that the misorientation between neighbouring dislocation cells varies. To investigate the character of the boundaries, misorientation is measured across the DDWs in the ferritic portion of the grain; see Figure 17A. The

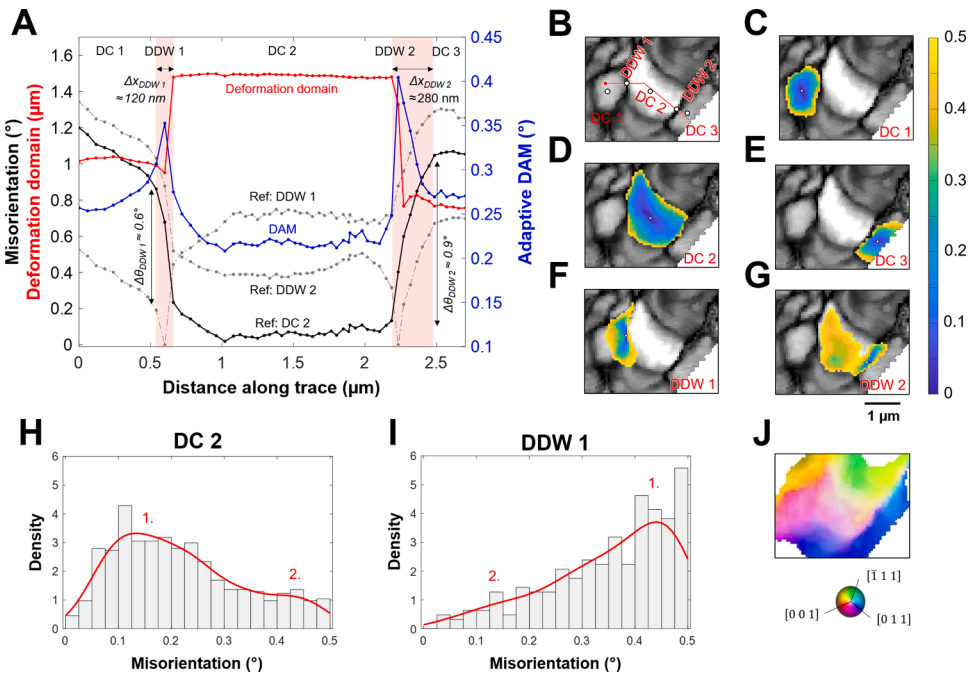

Figure 18. A) Trace of misorientation and kernel misorientation across two dense dislocation walls. The reference orientation is the average orientation of dislocation cell 2 (DC 2) and the points on the DDWs 1 and 2 as indicated in (B). B) Location of the trace (red) and the analysis points (white), C-G) Deformation domains and misorientations for reference points inside the dislocation cells (DC 1 – DC 3) and on the dense dislocation walls (DDW 1 – 2). H-I) Domain misorientation distributions for a dislocation cell (DC 2) and a dense dislocation wall (DDW 1). J) Rotation direction in the investigated domain, the colour key represents a maximum misorientation of 2° from the mean orientation of DC2.

misorientation values mostly vary between 0.3° – 1°, with an average misorientation of 0.62° for 100 measurements. Thus, average misorientation of the dense dislocation walls is in good agreement with the misorientation value $\Delta\theta_{DDW}$=0.5° used for the definition of the analysis. Approximately half of the measured DDW misorientations are overlaid on the adaptive DAM in Figure 17B. In general, the DDWs misoriented by more than 0.5° show very good contrast, while those misoriented by less than 0.5° appear slightly blurred. The appearance is expected to be dependent on the thickness and the misorientation gradient of the DDW.

To investigate the misorientation gradient of the DDWs, a region inside a sub-grain consisting of multiple dislocation cells is shown in Figure 18. A misorientation profile is shown between three dislocation cells using three reference orientations: the dense dislocation walls (DDW 1, DDW 2) separating the dislocation cells, and the average orientation of the middle dislocation cell (DC 2); see Figure Figure 18A for the profiles and Figure 18B for the reference locations. When the middle dislocation cell (DC 2) is the reference, it is clear that the orientation is quite uniform inside the DC2; see Figure 18D for the spatial misorientation distribution. The misorientation histograms for DC 2 and DDW 1 are shown in Figure 18H and Figure 18I. Two peaks can be identified from both distributions, one originating from inside the DC (1.) and the other from the DDW (2.). The proportions change considerably between the two examples, explaining the good dislocation cell contrast provided by the adaptive DAM ($\Delta\theta_{DDW}$=0.5°).

While the misorientation across DDW 1 is approximately 0.6° and approximately 0.9° across DDW 2, the boundary region is significantly thicker for DDW 2 ($\Delta x_{DDW\ 2}$) compared DDW 1 ($\Delta x_{DDW\ 1}$). Despite the wider transition at DDW 2, the adaptive DAM measures a distinct peak, located at the point of highest misorientation gradient. The gradual change in misorientation outside the boundary region of DDW 1 (boundary region is shaded in red) is the reason why the peak measured by adaptive DAM also broadens. The different character of the DDWs is also reflected in the shape of the deformation domains and in the misorientation distributions; see Figure 18F-G. Most of the DC 2 is included in the deformation domain for DDW 2, which is caused by the asymmetric misorientation profile having a misorientation lower than $\Delta\theta_{DDW}$=0.5° to DC 2. Despite the gradual change in misorientation, the transition between dislocation cells is captured effectively by the deformation domain's size (red trace in Figure 18A). These results show

Table 4
Estimated angular measurement noise and the global average kernel misorientations for the investigated structural steel indentations.

	Measurement noise (°)	Global average KAM, 1st nn (°)		
Dataset	Raw	Raw	De-noised	De-noising factor
Structural steel indentation 1	0.25	0.28	0.06	4.36
Structural steel indentation 2	0.37	0.39	0.05	7.90

that dense dislocation walls with varying misorientation gradients can be detected by the adaptive DAM. Furthermore, the adaptive DAM provides consistent misorientation values at the DDWs (e.g. 0.35 – 0.40° for DDW 1 and 2), which are also considerably higher than using conventional KAM (e.g. 0.23 – 0.24° for DDW 1 and 2), leading to an increase in the signal-to-noise ratio. The direction of material rotation relative to DC 2 also shows that there are multiple deformation domains rotating in different directions (Figure 18J), and these domains are consistent with the DCs shown in Figure 18B.

4.3. Sensitivity analysis

The quality of the EBSD data has a significant influence on how well the sub-structural deformation patterns can be resolved. Firstly, the angular measurement noise must be sufficiently low and preferably reduced with a de-noising filter; see Table 4 for measurement noise values of the structural steel indentations. Indentation 1 has a slightly lower level of measurement noise at 0.25° compared to 0.37° for Indentation 2. The estimated measurement noise is similar to the global average KAM value for the raw data. The half-quadratic de-noising reduces the noise level significantly, with both datasets showing similar global average KAM values at 0.05 – 0.06°. The de-noising factor is defined as the ratio of the global average KAM values, with noise reduction factors of approximately 4.4 and 7.9 for Indentation 1 and 2, correspondingly. The influence of measurement noise on the deformation patterns is shown in Figure 19 for Indentation 2. The sub-grain analysis using adaptive DMM (Figure 19A) shows speckle patterns and

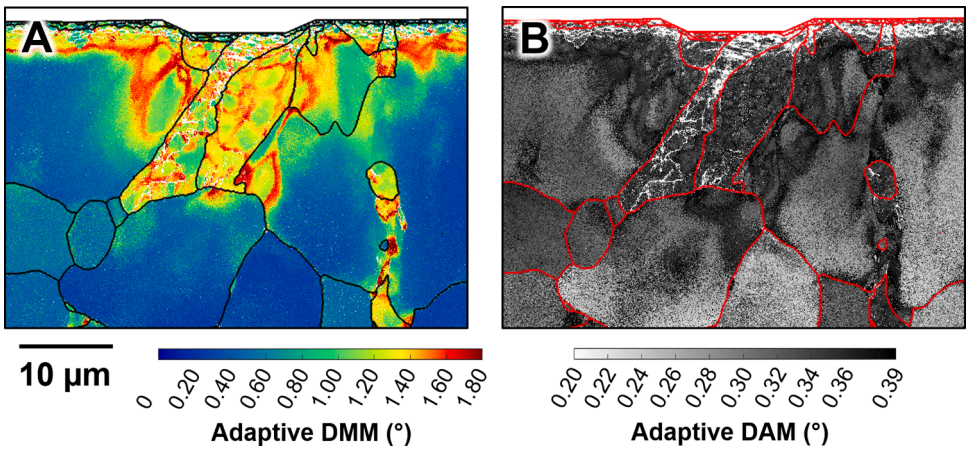

Figure 19. Adaptive domain misorientation for the structural steel indentation 2 using raw measurement data, showing: A) Sub-grain boundaries ($\Delta\theta_{SGB}$=*2.0*°) and B) Dislocation cells ($\Delta\theta_{DDW}$=*0.5*).

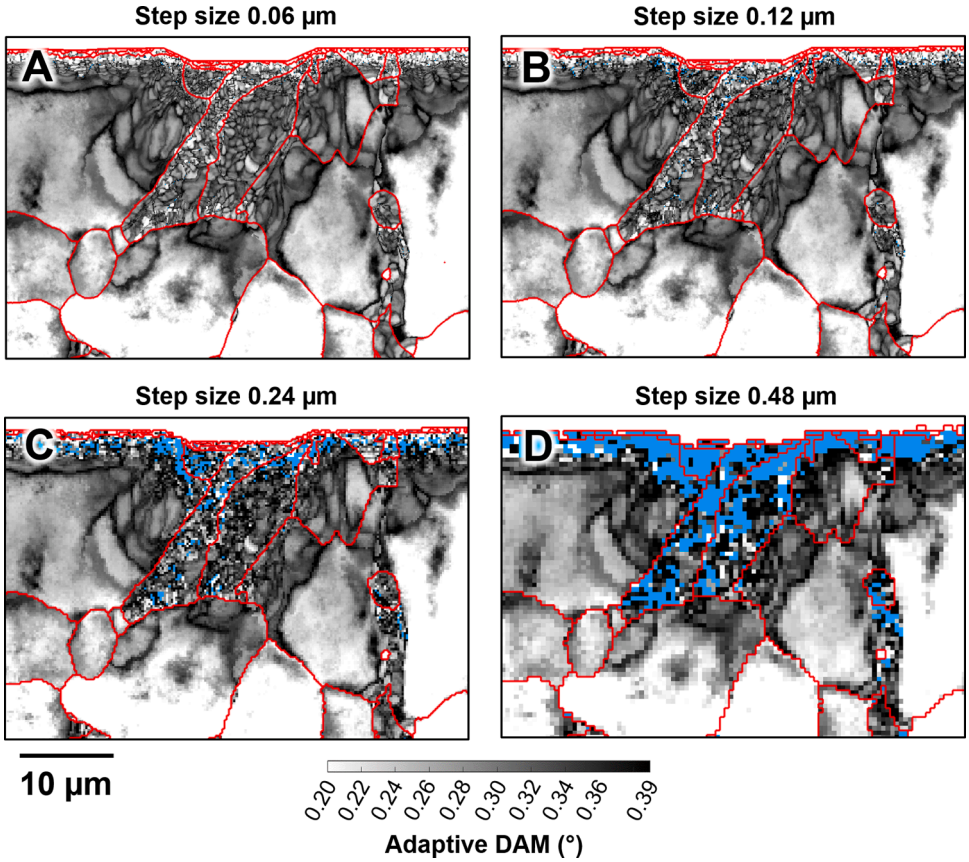

Figure 20. Influence of EBSD step size on the measurement of dislocation cells for structural steel Indentation 2 using Adaptive DAM ($\Delta\theta_{DDW}$=*0.5*°). The de-noised dataset is reduced by factors of 2, 4 and 8, resulting in step sizes of 0.12 µm, 0.24 µm and 0.48 µm, correspondingly. Blue colour indicates locations where no neighbouring datapoints are within the misorientation value $\Delta\theta_{DDW}$=*0.5*°.

elevated noise levels in the undeformed grains, but is otherwise very similar to the de-noised data shown in Figure 14B. The speckle pattern becomes more apparent for dislocation cell analysis (Figure 19B), and it partially obstructs the finest dislocation cells. Still, the larger deformation patterns are clearly visible on both flanks of the indenter and show good agreement with the de-noised results (Figure 15A). Especially the deformation domain size measurement can resolve the dislocation cells from as-measured Hough-based EBSD data; see Appendix A for further details.

Sensitivity of the dislocation cell analysis ($\Delta\theta_{DDW}$=*0.5*°) to spatial resolution is shown in Figure 20. The de-noised data is reduced by factors of 2, 4 and 8, resulting in step sizes of 0.12 µm, 0.24 µm and 0.48 µm, respectively. At the step size of 0.12 µm the adaptive DAM remains very similar even in the area of finest dislocation cells; see Figure 21A for the cumulative distributions in the highly deformed grain. At 0.24 µm step size the large dislocation cells are still visible on both sides of the indentation, but the heavily deformed grain has a significant loss of detail. This is expected, as the average dislocation cell size is approximately three times the step size of 0.24 µm; see Appendix B. The physical limitations become clear at a step size of 0.48 µm, as no value could be

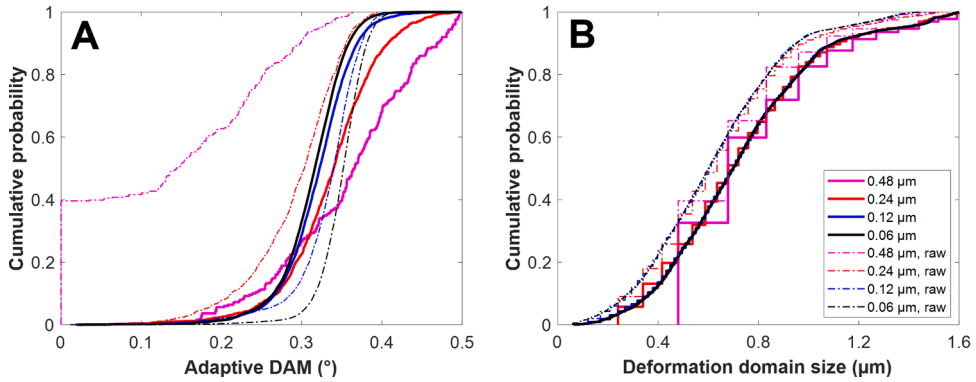

Figure 21. Cumulative probability distributions for the heavily deformed grain in Indentation 2, showing the distribution of A) Adaptive DAM, and B) size of the deformation domain. The solid lines represent the de-noised data in Figure 20, while the analysis for raw data is shown with the dash-dotted line.

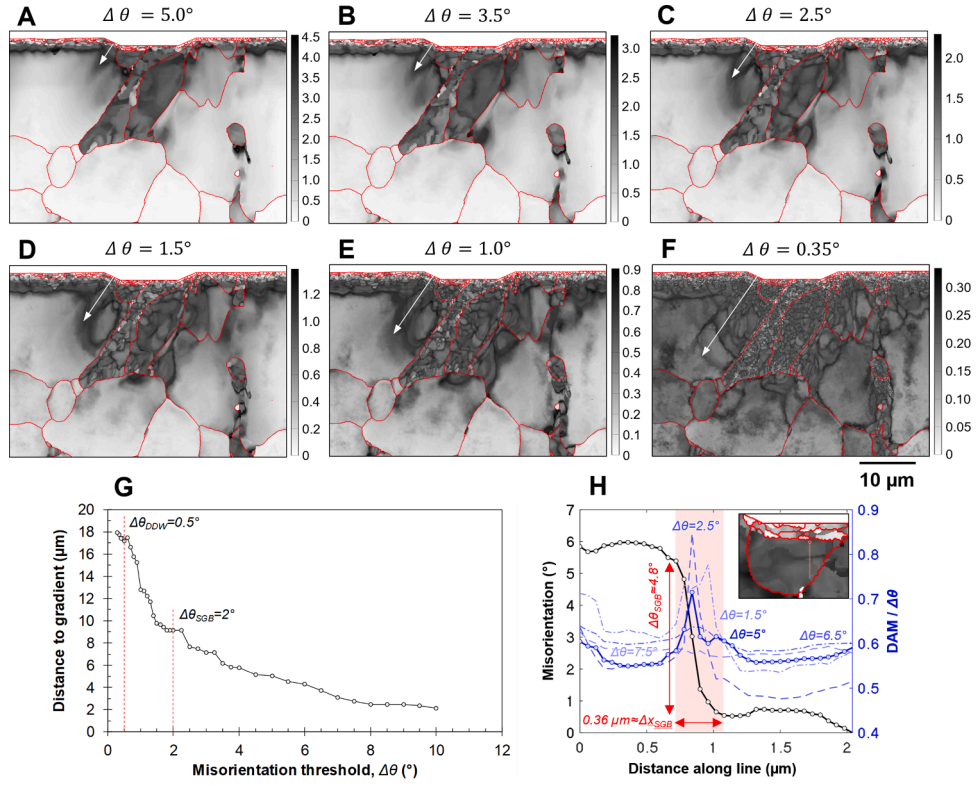

Figure 22. A-F) Adaptive DAM for indentation 2 at a varying misorientation values $\Delta\theta$ =0.35° – 5° (kernel size 12.06×12.06 μm). G) Distance to the furthest detectable orientation gradient on the left side of the indenter, shown by the white arrows in A-F. H) Trace of misorientation and DAM analyses with different $\Delta\theta$ values. The inset shows a close-up of the $\Delta\theta$=5° analysis.

calculated for many datapoints (see blue colour in Figure 20D). This is caused by two factors: 1) small size of dislocation cells, and 2) misorientation gradient that is larger than 0.5°/0.48μm = 1.04°/μm. Still, despite the limitations imposed by reduced spatial resolution and angular measurement noise, the deformation domain's size distribution remains very similar for the heavily deformed grain (Figure 21B). This shows that the sampled area remains consistent regardless of step size, as long as its sufficiently small in relation to the size of the features, allowing the location of the misorientation gradients to be detected. Furthermore, the scalar values of adaptive DAM remain relatively unchanged at all step sizes when calculation is possible. Refer to Appendix A for more details on the sensitivity analysis, including visual representations of the deformation domain size at reduced spatial resolution (e.g. Figure A-5).

The parameter that bears the most influence on the resolved deformation patterns is the misorientation value $\Delta\theta$, as exemplified by the different density of sub-structures resolved by $\Delta\theta_{DDW}$=*0.5* and $\Delta\theta_{SGB}$=*2*°. While the selection of the specific misorientation values is supported by directly measured values available in the literature, a sensitivity analysis was carried out in the range 0.35° – 10° in 39 discrete steps. The full analysis is provided in the Supplementary Video 2, and relevant sections of that are shown in Figure 22 for the range 0.35° – 5°. At large misorientation values $\Delta\theta$>*5*° no sub-structural boundaries are resolved, with the method measuring global misorientation gradients within the grains. Some sub-granular boundaries start to become visible in the 3.5 – 5° range, especially in the small grain under the indenter. Analysis shows that the first detected boundary has a misorientation of $\Delta\theta_{SGB}$=4.8° across the boundary, see Figure 22H. The first misorientation value that produces a clear peak at this sub-grain boundary is $\Delta\theta$=*5*°. The best contrast is achieved at $\Delta\theta$=*2.5*°, which is approximately

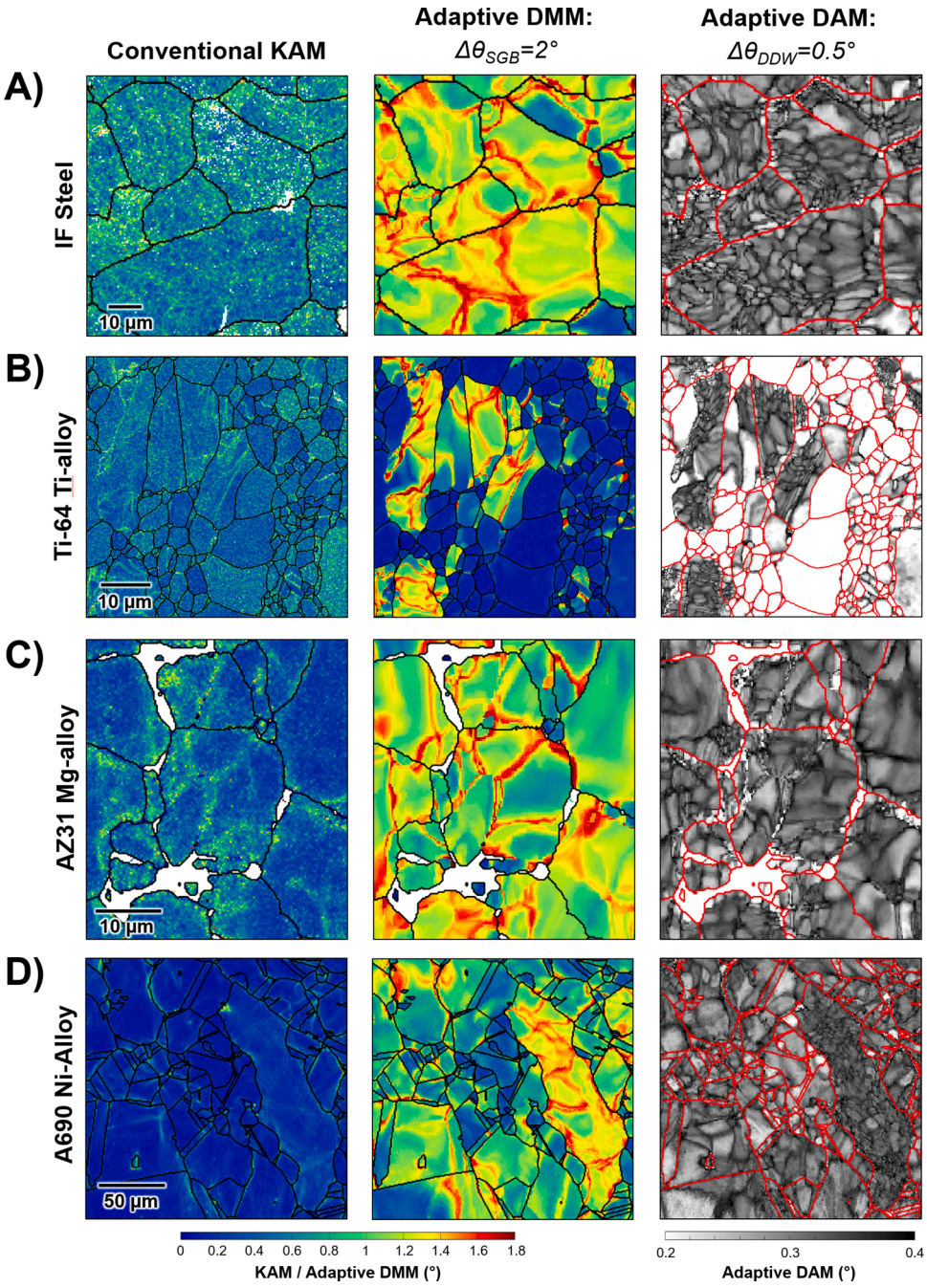

Figure 23. Open EBSD data for A) deformed interstitial free steel, B) Ti-64 titanium alloy, C) AZ31 magnesium alloy strained to 2%, D) A690 nickel alloy strained to 2%. Conventional KAM uses as-measured orientation data. The kernel size for adaptive DAM and DMM is 60 nearest neighbours for all cases, which is large enough to cover the largest grains. Grain boundaries are overlaid in black or red.

half of the $\Delta\theta_{SGB}$. The other sub-granular boundaries start to become visible at $\Delta\theta$=2.5°, without major changes until approximately $\Delta\theta$=1.5°.

A clear reduction in the size of the deformation patterns is observed at $\Delta\theta$=1°, which is consistent with the observation of Tao et al. [14] that DDW's typically have a misorientation smaller than 1°. There is a continuous refinement of the sub-structure until approximately $\Delta\theta_{DDW}$=0.5°, at which point smaller misorientation values no longer cause major changes to the resolved deformation patterns. The dislocation cell structure refines slightly at smaller values, however, $\Delta\theta$=0.35° is already being limited by the angular and spatial resolution of the dataset. In particular with such small misorientation values, the deformation domains are not always limited by physical boundaries, but rather the misorientation gradient at any given point. For this reason, measurements on DDWs may only sample material along the DDW, and not the misorientation gradient between two dislocation cells. This will create an artefact in which a DDW will appear to split into two DDWs with an area of low misorientations in the middle, being somewhat similar to a small dislocation cell. These artefacts can be detected in two ways: 1) Deformation domain is very narrow and elongated, matching the shape of the DDW determined at a slightly higher $\Delta\theta$ value, and 2) There is a local orientation gradient detected by conventional KAM (1st nn, θ_{max}=2°, de-noised data) at the location of low DAM. It has been checked that this effect is minimal for the current experiments using $\Delta\theta_{DDW}$=0.5°. Furthermore, residual deformation in the material, be it due to processing or sample preparation, interferes with the analysis of the small misorientation values.

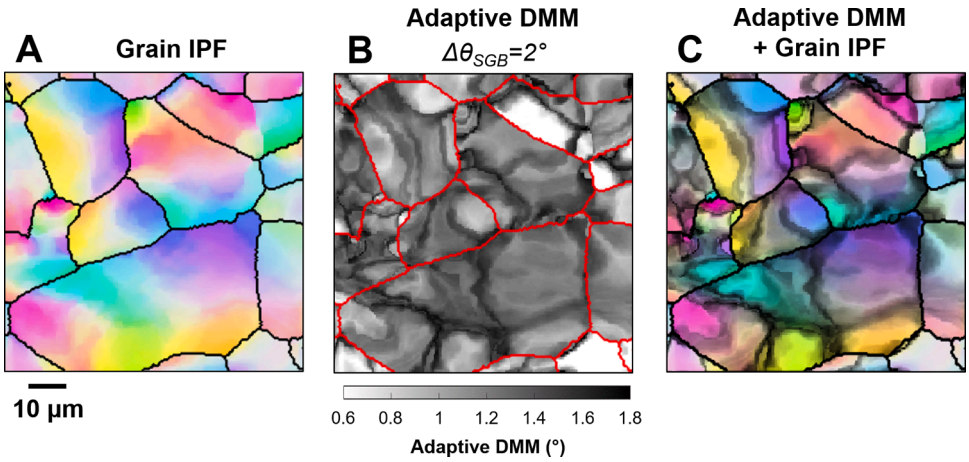

Figure 24. A) Grain-based orientation map for the interstitial free steel, refer to Figure 10 for the colour key. B) Adaptive DMM showing the locations of the sub-grain boundaries, C) Sub-grain boundaries resolved by adaptive DMM overlaid on the grain-based orientation map.

To give a rough quantification of the changes induced by varying $\Delta\theta$, the distance to the furthest detectable location of high misorientation gradient is measured on the left side of the indentation, shown by the white arrows in Figure 22A-F. As shown in Figure 22G, the distance remains constant between $\Delta\theta$=8 – 10°, and then showing a continuous increase until approximately $\Delta\theta$=3.25°. After a short plateau, a second plateau is observed between 1.6 – 2.25°. With smaller values the distance quickly increases, stabilizing at $\Delta\theta$=0.6°. Thus, should the parameters $\Delta\theta_{DDW}$=0.5° and $\Delta\theta_{SGB}$=2° be used for measuring the size of the deformation field, the results would remain mostly unchanged in the neighbourhood of the misorientation value. It is emphasised that this is a simple quantification to show the influence of the misorientation value in the particular case, and comparative studies using TEM are required to study how well the results correspond with direct observations of varying dislocation sub-structures.

4.4. Sub-structural analysis for various deformed metals

The adaptive domain misorientation is applied to open access literature EBSD datasets of various deformed metals in Figure 23. For the IF steel dataset shown in Figure 23A, no patterns are resolved by conventional KAM due to measurement noise; see Appendix A for estimated measurement noise levels of the literature datasets. On the contrary, the adaptive DMM reveals a network of sub-grain boundaries. Deformation is high in all grains shown, with some differences in the size of the sub-grains. While some sub-grain boundaries seem overly thick e.g. in the large grain at the bottom, the deformation domain measurement in Appendix A shows sharper boundary locations. The adaptive DAM reveals fine dislocation cells, with their size varying considerably in different locations. While the spatial resolution is not high enough to resolve all details, most sub-structures are clearly visible.

The Ti-64 Titanium-alloy in Figure 23B has deformation patterns resolved by the conventional KAM. However, the patterns are masked by the measurement noise showing up as speckle patterns, making it difficult to determine which grains are deformed. The sub-grain analysis shows the effectiveness of the adaptive DMM, resolving highly deformed grains with sub-granular boundaries as well as undeformed grains. The undeformed grains correspond to the grains with a speckle pattern in the conventional analysis. The measurement noise is effectively reduced by the half-quadratic filter, reducing the adaptive DMM to less than 0.2° for the undeformed grains. The adaptive DMM remains mostly unchanged with as-measured data, however, the speckle pattern persists; see Appendix A for adaptive DMM analysis of all as-measured datasets. Using the de-noised data fine sub-structures are also resolved by the adaptive DAM.

For the AZ31 Mg-alloy (Figure 23C) the sub-grain boundaries become much clearer with adaptive DMM in comparison to the conventional KAM. In addition, several new sub-grain boundaries become visible. While the spatial resolution of the data is limited, the adaptive DAM resolves a large amount of sub-structures that are significantly finer than the sub-grains. For example, the grain in the top-right corner shows the sub-division of the grain that is not resolved either by the

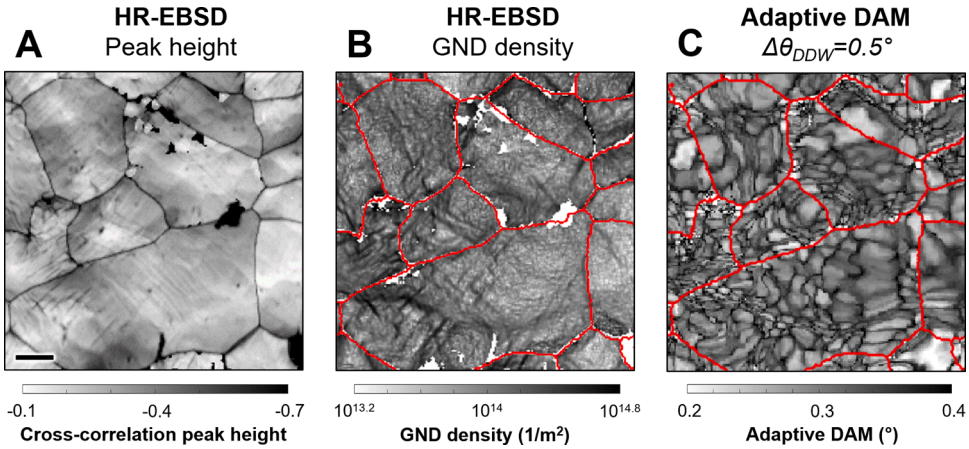

Figure 25. Cross-correlation based HR-EBSD data [59] showing: A) cross-correlation peak high that is analogous to EBSD image quality, and B) total geometrically necessary dislocation density. C) the dislocation cell structure resolved by the adaptive DAM. The scale bar in sub-figure A is 10 µm in length.

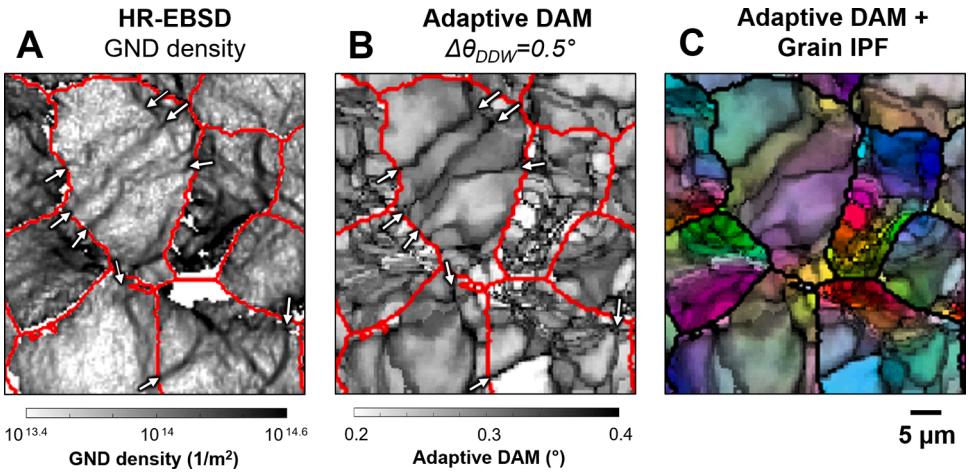

Figure 26. Cross-correlation based HR-EBSD data [59] showing: A) total geometrically necessary dislocation density. B) The dislocation cell structure resolved by the adaptive DAM. C) Overlay of the dislocation cell structure (B) on the grain-based orientation map.

adaptive DMM or the conventional KAM.

The fourth dataset is the A690 Nickel-alloy (Figure 23D) with a low measurement noise level, requiring no post-processing for the analysis. The high quality of the data is shown in the conventional KAM as a low noise floor compared to the other datasets. Deformation seems to have localised in the large elongated grain on right side, however only few sub-structural details are resolved with conventional KAM. The adaptive DMM reveals a network of sub-grain boundaries for the elongated grain. The adaptive DAM shows fine dislocation cells in this grain, with larger dislocation cells resolved in other areas of the EBSD map. Both adaptive DMM and DAM reveal differences in the degree of deformation for different grains, both through the average misorientation value and the size of the sub-structures. This is the only dataset of the four, where DDW's can be measured from the raw data. The dataset has very low measurement noise estimated at 0.09°; see Appendix A for further details. It can be concluded that the adaptive domain misorientation approach effectively captures the formation of heterogeneous deformation patterns and grain sub-structures for a variety of deformed metals.

4.5. *Comparison with other electron microscopy methods*

This section is focused on comparing the deformation patterns resolved by adaptive domain misorientation approach to the features resolved by other EBSD analysis methods. This will increase the confidence in the methodology if different sampling and analyses approaches can resolve similar deformation patterns. First, the grain-based misorientation map for the interstitial free steel clearly shows deformation patterns as regions of similar colour (Figure 24A). The sub-granular boundaries resolved by adaptive DMM (Figure 24B) are displayed on top of these patterns in Figure 24C. While the resolved sub-grain boundary locations are slightly blurred, they match up extremely well with the rotational patterns such that the colour is uniform inside the sub-grains. This indicates that the crystal lattice is rotating in similar global directions inside the entire sub-grains, as would be expected. The fluctuations in grain IPF's colour and adaptive DMM's values inside the sub-grains are an indication of the dislocation cell structure.

Next the locations of sub-grain boundaries and dense dislocation walls are compared to the HR-EBSD results [59] of the interstitial free steel. The cross-correlation peak height in Figure 25A is analogous to the image quality maps used in conventional EBSD, showing wavy slip traces inside the grains. The total geometrically necessary dislocation (GND) density in Figure 25B shows clear deformation patterns inside the grains. In general, the sub-grain boundaries resolved by adaptive DMM (Figure 24B) coincide with high dislocation density, even though most of these boundaries are not very prominent in the HR-EBSD data. The GND density plot resolves fine sub-structures, and many patterns coincide with the dislocation cells resolved by the adaptive DAM (Figure 25C). However, this is not apparent in many locations due to the noisy appearance of GND density and requires swapping between overlaid images.

An additional subset of the same EBSD dataset is shown in Figure 26 for further comparison to the adaptive domain misorientation. In this subset several dense dislocation walls can be identified from both datasets, highlighted by the white arrows. Furthermore, the areas of the finest dislocation cells correspond with the grains that have the highest dislocation densities. The dislocation cells resolved by the adaptive DAM are overlaid on the grain-based orientation map in Figure 26C. To enhance contrast, full colour saturation represents a 7.5° misorientation from the grain's mean orientation. This shows that the areas confined by the DDWs have quite uniform rotation. This is especially the case for the grain at the top (arrows in Figure 26B), which has low GND density and no sub-grain boundaries resolved by adaptive DMM (not shown). For grains with high GND density, e.g. the green-purple grain on the left side, neighbouring dislocation cells share similar rotation directions. In this case the green and purple regions represent two sub-grains, and the global misorientation gradient of the sub-grains hides the rotation directions of the individual dislocation cells in the grain-based misorientation analysis.

5. Discussion

The current work developed an adaptive domain misorientation approach, which utilises unconventionally large measurement domains for local misorientation analysis. Contrary to the conventional KAM using a step-size dependent, nearest neighbour definition for the kernel size [31], the current study adapts the measurement domain to the size and shape of the dislocation sub-structures. This strategy was shown to be effective for resolving deformation patterns and categorizing the sub-structural boundaries according to misorientation across the boundary region with a varying thickness. In the following sub-sections, the key issues related to local misorientation analysis and deformation pattern measurement are discussed. Furthermore, a comparison of different EBSD analysis methods is presented, and recommendations are given for future work.

5.1. *Influence of spatial and angular resolution*

While the conventional KAM is effective for measuring the global level of deformation, the sensitivity to EBSD's spatial and angular

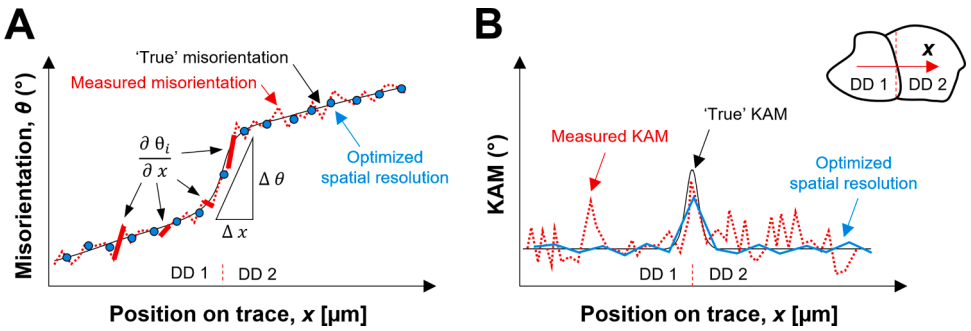

Figure 27. Trace of A) Misorientation, and B) Conventional KAM between two deformation domains characterised by a change in the misorientation gradient at the interface.

resolution [31,35,67] limit its ability to resolve the dislocation sub-structures. To improve the quality of classical EBSD-based analysis, different noise reduction strategies have been applied to Hough-based EBSD data in order to improve the signal-to-noise ratio [37–41]. Recently, Bergmann et al. [38] have introduced a half-quadratic de-noising approach that removes spatially independent noise effectively. In the current study the half-quadratic filter achieved noise reduction factors of 4 – 8 for the structural steel indentations, while still retaining the small local changes of the misorientation gradient (Table 4). Further improvement in angular resolution can be achieved by using a pattern-matching algorithm for the determination of crystal orientation [68–72]. For example Nolze et al. [68,69] used a pattern-matching approach to improve the angular resolution to approximately 0.05°. While both de-noising and pattern-matching provide a lower noise floor for the measurement, the measurement of sub-structures still has limitations imposed by the nearest neighbour sampling principle.

The dependencies between resolution, misorientation gradient and conventional KAM are presented schematically in Figure 27, which shows traces of misorientation and conventional KAM across two deformation domains. For simplicity, misorientation is assumed to increase monotonically, with a constant misorientation gradient inside the deformation domain and a variable high gradient at the interface; see Figure 27A. Because of the angular measurement noise, the gradient $\partial\theta_i/\partial x$ varies between adjacent measurement points. Depending on the magnitude of measurement noise and the spatial resolution, similar KAM values may be measured inside the deformation domains and at the interfaces; see Figure 27B. When the interiors of the deformation domains are considered, the spatial resolution dependence of KAM is the relationship of true orientation change between measurement points in relation to the measurement noise. By increasing the distance between measurement points the true orientation change increases, reducing the influence of angular measurement noise. This leads to smaller fluctuations in KAM, and the scalar value begins to be a better representation of the actual misorientation gradient at a given point. At interfaces the conventional KAM will highlight the boundaries with a high misorientation gradient. The highest values are measured for boundaries where boundary region thickness Δx is approximately two times the step size, and $\Delta\theta$ is slightly less than two times the threshold angle θ_{max} for excluding measurements. Thus, highly misoriented sub-grain boundaries will be highlighted by large θ_{max} values, and DDWs are highlighted by low θ_{max} values albeit measurement noise becomes an issue.

At the interfaces the spatial resolution can be optimized by maximizing the misorientation gradient $\Delta\theta/\Delta x$. However, as spatial resolution is decreased to potentially increase $\Delta\theta$ between adjacent points, it is less likely that the optimal spatial arrangement shown in Figure 27A is achieved. To overcome the detrimental effects of spatial resolution reduction, Kamaya [35] proposed the extended local misorientation -concept. While this clever global optimization strategy yields a better signal-to-noise ratio while maintaining spatial resolution, a local optimization strategy would be even more effective. This is particularly the case for different dislocation sub-structure types, as they inherently have different $\Delta\theta/\Delta x$ relationships and Δx will also vary for sub-structural boundaries of the same type as shown in Figure 18A and Figure 22G. In the developed domain misorientation approach the local optimization of sampling is achieved by growing the measurement area radially until the misorientation value $\Delta\theta$ has been reached. The particular advantage of this is that no prior knowledge is required about the boundary region thickness Δx; the adaptivity of the deformation domain is able to capture both gradual and sharp changes in misorientation, as shown by Figure 18A.

Another interesting aspect of the developed approach is that the misorientation values (DAM, DMM) do not directly describe the misorientation at a given point, but instead are an effective proxy for detecting the locations of large misorientation gradients. Based on this information, more accurate analyses can be performed to characterise the sub-structures; see e.g. Figure 17 and Figure 18. The contrast provided by DAM for DCs and DDWs is very good, as the difference in misorientation gradient is significant (Figure 16C and Figure 18A). Based on Figure 18A, the average curvature is 5°/µm and 3.2°/µm for DDW 1 and DDW 2, compared to a maximum of 0.6°/µm inside DC 1 and DC 2. Locations of sub-grain boundaries are not always defined as sharply by DMM for two reasons. First, the orientation gradients can extend to the neighbourhood of the sub-grain boundary as shown in Figure 12. Second, the sampling of numerous dislocation cells (Figure 12G) within a sub-grain creates a wide misorientation distribution. This is particularly the case for large grain sizes, where the misorientation distribution inside the sub-grain may be larger than $\Delta\theta_{SGB}$=2°, affecting for example the IF steel shown in Figure 23A. As a result, DMM will increase inside the sub-grain for a given misorientation gradient when the sub-grain size increases, reducing contrast to the sub-grain boundaries. The analysis for sub-grain boundaries could be enhanced by considering how the proportions of the multi-modal distributions change (Figure 12D-F), or by exploiting the consistency of rotation direction on the sub-grain boundary (Figure 12G-I). Furthermore, information about lattice curvature could be recovered for sub-grain interiors. The information about curvature would be particularly valuable, as the lattice curvature based deformation model by Tóth et al. [8] was able to capture the evolution of dislocation density, texture and grain refinement for a severe plastic deformation process. These are all key aspects to understanding how energy is dissipated in the microstructure during plastic deformation.

5.2. *Classification of sub-structural boundaries*

In order to understand the role of grain refinement in the energy dissipation process, the grain sub-structures need to be classified. As described in Section 5.1, the scalar values of conventional KAM reflect the misorientation gradient, i.e. lattice curvature, but are affected by spatial and angular resolution. In particular, the KAM values are

Table 5
Features resolved by the adaptive domain misorientation approach and other scanning electron microscopy methods utilised in the current research.

Method	Features resolved					
	Global strain comparison	Strain localisation	Sub-GBs	DDWs	Dislocation cell size	Rotation patterns
Conventional KAM	x	x [a,b]	x [a,b]	x [a,b,c]	–	–
Adaptive DMM ($\Delta\theta_{SGB}$=2°)	x	x	x	–	–	–
Adaptive DAM ($\Delta\theta_{DDW}$=0.5°)	x [a]	x [a]	–	x [a, c]	x [c]	–
Grain IPF	x	x	x [b]	x [b,c]	–	x [b]
HR-EBSD GND density	x	x	x [a]	x [a,c]	–	–

a) Measurement noise blurs details, de-noising recommended
b) Influenced by global orientation gradients
c) High spatial resolution required

dependent on step size and thickness of the sub-structural boundary region (Δx), and thus it is not suitable for the classification of the sub-structures. The adaptive domain misorientation approach (DAM and DMM) resolves this issue by categorizing the boundaries according to the total misorientation across the boundary region. The sensitivity analysis (Figure 22) showed that a sub-grain boundary with $\Delta\theta_{SGB}$=4.8° is first visible at $\Delta\theta$=5°. Highest contrast was provided at $\Delta\theta$=2.5°, which is approximately half the sub-grain boundary misorientation. This provides insight to the deformation patterns that are resolved at different $\Delta\theta$ values; the boundaries resolved by a specific $\Delta\theta$ are typically misoriented approximately between θ and 2θ. This is also visible in the dislocation cell analysis (Figure 17), as 90% of the boundaries are misoriented between 0.36° – 0.96° for the misorientation value $\Delta\theta_{DDW}$=0.5°. The average misorientation in this case was 0.62°, being slightly higher than $\Delta\theta_{DDW}$. The misorientation values $\Delta\theta_{DDW}$=0.5° and $\Delta\theta_{SGB}$=2.0° were used in this study to resolve two levels of sub-structural configurations, representing the dislocation cells and sub-grain boundaries. These two misorientation values can be used to represent the general progression of plastic deformation by measuring the size distribution of the different sub-structures. This is supported by the work of Pantleon [43] and Estrin [44], who have shown that misorientation accumulates progressively between DCs as strain increases, leading to the formation of a fine-grained microstructure as shown in Figure 1. For this reason, the size of the dislocation cell structure in the early phases of deformation is indicative of the achievable degree of grain refinement under large strain [73,74]. The size distribution of the dislocation cells is also an indicator of the level of deformation [21,22], and it can be measured by the adaptive domain misorientation approach without defining the pixel-to-pixel boundary locations as required in conventional grain size analyses [49,50]. A comparison of deformation domain size and dislocation cell size is presented in Appendix B. This is a promising result, as usually TEM is required to study the size distribution of dislocation cells [14], which has the drawback of being limited to small regions of interest. The size of the deformation domain was also shown to provide an excellent representation of the dislocation cell structure even at reduced spatial resolutions (Figure 16A and Figure A-5).

5.3. Comparison of EBSD analysis methods and future work

The adaptive domain misorientation approach was successfully applied to several deformed metals (Figure 23) and combined with other analysis methods, showing the versatility of the approach; see Table 5 for an overview of the characteristics of different methods. The main limitation of conventional KAM is its sensitivity to measurement noise. The quality of EBSD data is of utmost importance for all methods, but the adaptive domain misorientation approach is more tolerant to measurement noise than conventional KAM. While the classification of the sub-structural boundaries is ambiguous using the scalar KAM values, the adaptive DAM and DMM classify the sub-structures according to the total misorientation across the boundary region ($\Delta\theta$). In addition, the scalar values of adaptive DAM and DMM don't seem to be influenced by the global misorientation gradient, producing quite uniform values at the sub-structural boundaries regardless of distance to the indenter (e.g. Figure 11C, Figure 15A). On the contrary, conventional KAM is considerably higher closest to the indenter due to the global misorientation gradient (Figure 11B). The grain-based and HR-EBSD analyses are complementary to the information provided by the adaptive domain misorientation. In particular, the deformation patterns provided by grain-based analyses (grain IPF) are very useful in combination with the adaptive domain misorientation (Figure 12G-H, Figure 24C and Figure 26C) for the verification of the sub-structures. The comparison in Figure 24C showed that material rotation is consistent inside the sub-grains determined by adaptive DMM. This is in agreement with the work of Humphreys [75], where a sub-grain was defined as a region containing material that is within a (small) specific misorientation range. Similar consistent rotation directions were also observed inside dislocation cells in this study, as shown in Figure 18J and Figure 26C. While the comparison to HR-EBSD based dislocation density (Figure 25 and Figure 26) showed reasonable agreement with the adaptive domain misorientation, the noise level of the dislocation density measurement made the comparison challenging. Still, several sub-structural boundaries correspond between the two datasets, especially in Figure 26. Furthermore, the grains with high dislocation densities have sub-grain boundaries and fine dislocation cells (Figure 25), while those with low dislocation densities only have noticeably larger dislocation cells (Figure 26). To further improve the dislocation density comparison, the noise reduction approach by Ruggles et al. [76] could be utilised to reduce the noise level of HR-EBSD dislocation density measurement by approximately one order of magnitude. Further study is required to compare deformation patterns resolved by the adaptive domain misorientation to electron channeling contrast imaging (ECCI) and direct TEM observations. While the current study focused on observing the deformation patterns in metals, the methodology could also be applied to other inorganic materials with dislocation-mediated deformation processes, for example in the fields of geology [77] and glaciology [78,79].

6. Conclusions

This work developed a novel domain misorientation approach for the measurement of deformation induced dislocation sub-structures. The chosen sampling strategy utilised adaptive measurement domains, which are grown radially to match the size and shape of the dislocation sub-structures. This approach proved to be effective for detecting the misorientation gradients between sub-structural features, and for measuring the misorientation characteristics (angle and direction) inside the sub-structural domains. It was shown that this approach can resolve deformation patterns for structural steel and various other deformed metals, classified according to the total misorientation across the sub-structural boundaries, denoted $\Delta\theta$. In the current study, the dense dislocation walls and sub-grain boundaries were resolved with misorientation values of $\Delta\theta_{DDW}$=0.5° and $\Delta\theta_{SGB}$=2.0°. The adaptive sampling approach was able to capture both sharp and gradual boundaries, with the thickness of the boundary region (Δx) varying from approximately 100 nm up to 280 nm for dense dislocation walls and

typically varying between 200 – 500 nm for sub-grain boundaries. The scalar misorientation values of the developed approach (DAM, DMM) were found to be stable regardless of spatial resolution, contrary to conventional KAM. Adaptive DAM was found effective for resolving dislocation cells and the adaptive DMM enhanced the contrast for sub-grain boundaries. The size distribution of dislocation cells could also be captured with the developed approach, which may be used for estimating the level of plastic deformation. Furthermore, the influence of spatial resolution and angular measurement noise on conventional and the developed approach were discussed; requirements for spatial and angular resolution were established based on the size and misorientation of the sub-structures.

Declaration of competing interest

None.

Acknowledgements

The present research was financially supported by the Academy of Finland (decision no. 298762), Aalto University School of Engineering, and the Finnish Maritime Foundation. This financial support is gratefully appreciated. Heikki Remes and Pasquale Gallo from Aalto University are gratefully acknowledged for comments on the manuscript. The work of Teemu Sarikka from Aalto University on EBSD acquisition of the datasets and general commenting is highly appreciated.

Supplementary materials

Supplementary material associated with this article can be found, in the online version, at doi:10.1016/j.ultramic.2021.113203.

Appendix A. Sensitivity to spatial and angular resolution

Spatial resolution

The basis for the spatial resolution sensitivity analysis is the step size dependence of conventional KAM. As step size increases for conventional KAM, the scalar values of KAM also typically increase; see Figure A-1. This makes the method sensitive to both the orientation gradient induced by the sub-structures, as well as the magnitude of misorientation at the sub-structural boundaries. Thus, the relationship between the value of KAM and the characteristics of the sub-structural boundary is ambiguous.

To demonstrate the robustness of the adaptive domain misorientation approach, a sensitivity analysis to EBSD spatial resolution is shown in Figure A-2. Compared to the domain misorientation of the full dataset in (A), the data is reduced by 50% (B) and 75% (C), resulting in respective step sizes of 0.2 μm and 0.4 μm. The dataset is reduced after de-noising to eliminate the influence of de-noising different datasets. The same physical kernel size is used in all analyses, corresponding to 12.1 μm (A), 12.2 μm (B), and 12.4 μm (C). The general outlook of deformation remains very similar at all step sizes. Naturally, the reduced spatial resolution at 0.4 μm step size makes distinction of the finest sub-grains at the top of the heavily deformed grain impossible. Still, the distribution of misorientation in that grain remains similar at all step sizes, as shown in Figure A-3A. The deformation domain size remains uniform at all step sizes, shown in Figure A-2D-F. The deformation domain's size distribution for the heavily deformed grain is shown in Figure A-3B, with very little difference observed between the three step sizes. Therefore, the iterative process for kernel size determination presented in Appendix C can be carried out with a reduced dataset.

Sensitivity to spatial resolution for the dislocation cell analysis ($\Delta\theta_{DDW}$=0.5°) of Indentation 2 is shown in Figure 20. As previously, the

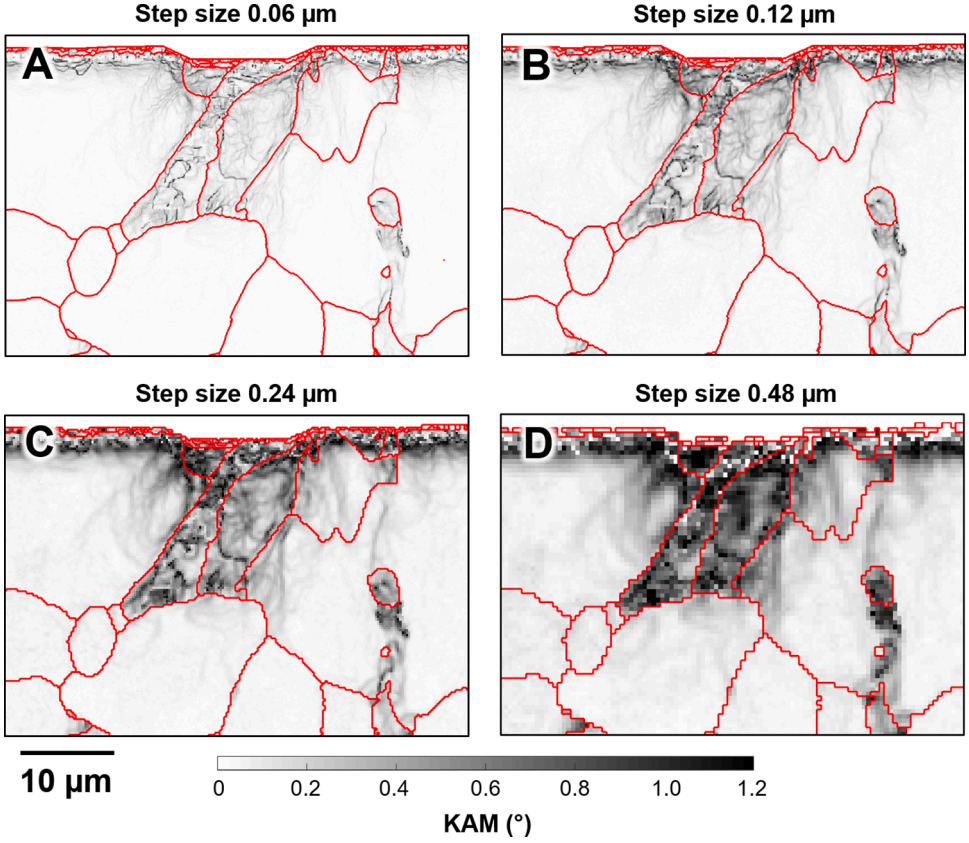

Figure A-1. Spatial resolution dependence of conventional KAM for Indentation 2 (de-noised data), using step sizes: A) 0.06 μm, B) 0.12 μm, c) 0.24 μm, D) 0.48 μm.

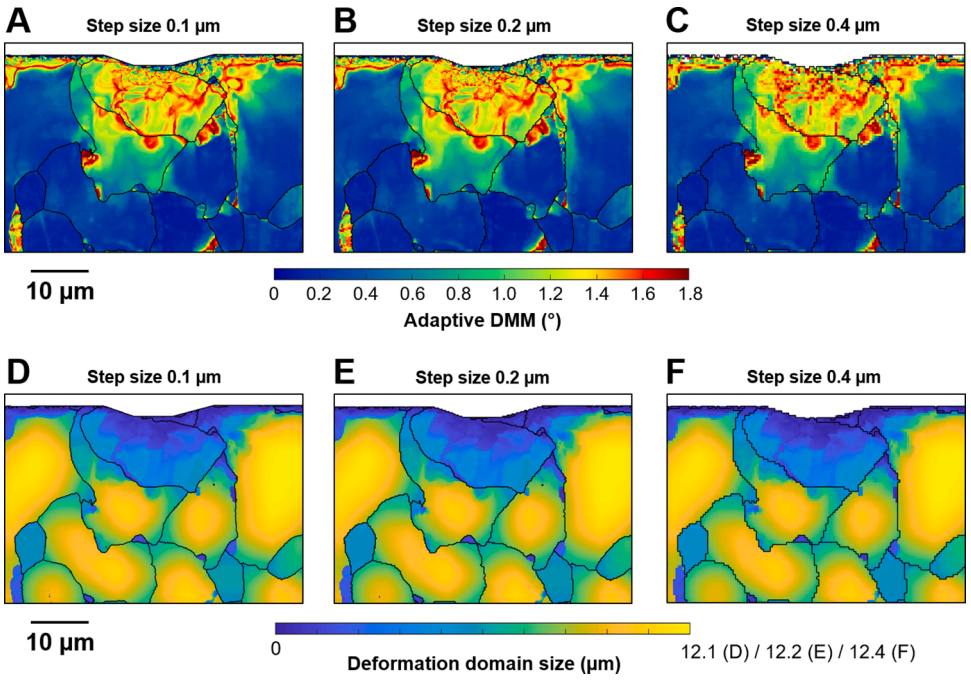

Figure A-2. Influence of EBSD step size on measurement of sub-grains for structural steel Indentation 1. The original dataset is reduced by factors of two and four, resulting in step sizes of 0.2 μm and 0.4 μm, correspondingly: A-C) Adaptive DMM ($\Delta\theta_{SGB}$=2°) for a kernel size of 12 μm (within step-size accuracy), D-F) Deformation domain size corresponding to A-C.

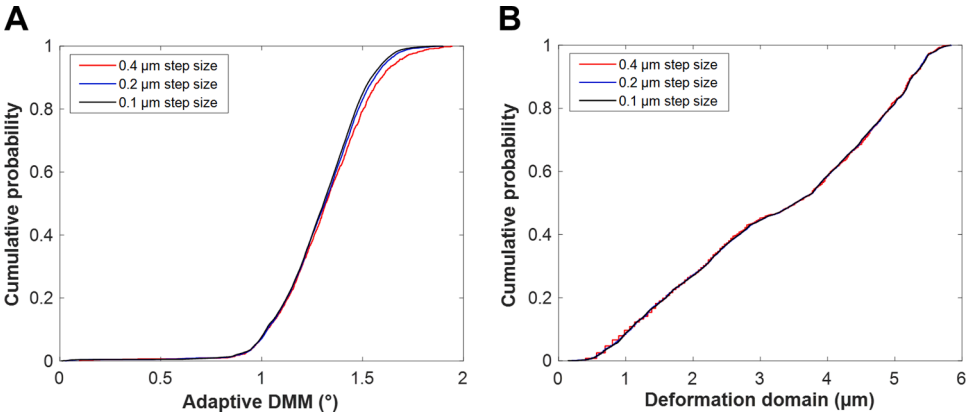

Figure A-3. Cumulative probability distributions for the heavily deformed grain in Figure A-2, showing the distribution of A) Adaptive DMM ($\Delta\theta_{SGB}$=2°), and B) Size of the deformation domain.

data is reduced by factors 2, 4 and 8, resulting in step sizes of 0.12 μm, 0.24 μm and 0.48 μm, correspondingly. At step sizes of 0.06 μm and 0.12 μm the adaptive DAM remains very similar even in the area of finest dislocation cells; see Figure 21A for the distributions. At 0.24 μm step size the large dislocation features are still visible from adaptive DAM on the left and right side of the indentation, but the heavily deformed grain has a significant loss of detail. This is expected, as the average dislocation cell size is approximately three times the step size; See Appendix B. Despite the reduction in spatial resolution, the deformation domain size in Figure A-4 remains very similar at all step sizes. The size distributions in Figure 21B are very similar, with increased staircasing at larger step sizes. Still, the shapes of the distributions are nearly identical, which is beneficial for estimating the size distribution of dislocation cells. As such the deformation domain can visualise the dislocation cell structure with relatively low spatial resolution when the adaptive DAM no longer resolves the details. As shown in Figure A-5, many of the dislocation cells are still resolved at the 0.24 μm step size. Thus, it can be concluded that the adaptive domain misorientation approach samples material consistently at different spatial resolutions, and can recover details of the dislocation cell structure at relatively low spatial resolution in relation to the size of the sub-structures. The scalar values of adaptive DAM remain nearly unchanged despite the step size, and is made obvious when comparing Figure 20 and Figure A-1.

Angular resolution

The sub-grain analysis for Indentation 1 mapped at 0.1 μm step size is shown in Figure A-6. The adaptive DMM analyses (A, B) are very similar, with some speckle patterns and elevated noise levels for the raw data (B). The deformation domain measurements (C, D) are however nearly identical, showing its robustness against measurement noise. The same observations hold for Indentation 2 mapped 0.06 μm step size, shown in Figure A-7. This measurement has more speckle pattern noise, indicating that indexing was not as consistent. This is reflected in the estimated

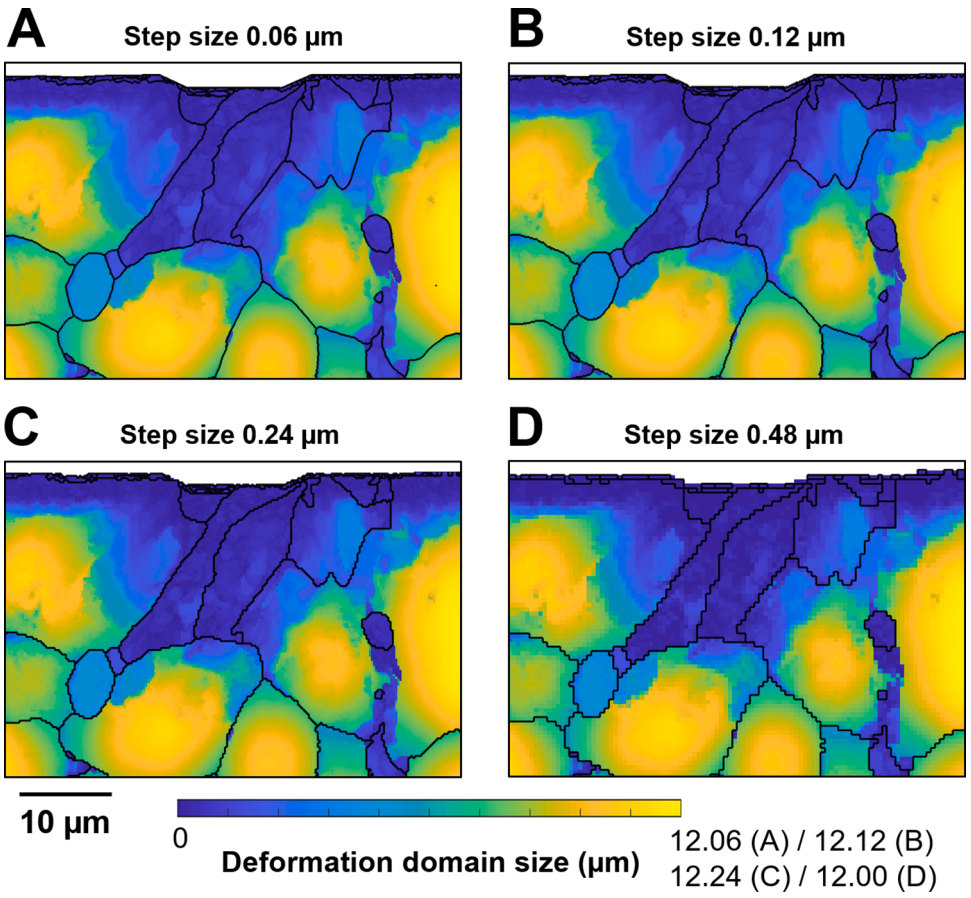

Figure A-4. Influence of EBSD step size on the measurement of deformation domain for structural steel Indentation 2 using Adaptive DAM ($\Delta\theta_{DDW}$=0.5°, kernel size 12 µm within step-size accuracy). The original dataset is reduced by factors of 2, 4 and 8, resulting in step sizes of 0.12 µm, 0.24 µm and 0.48 µm, correspondingly.

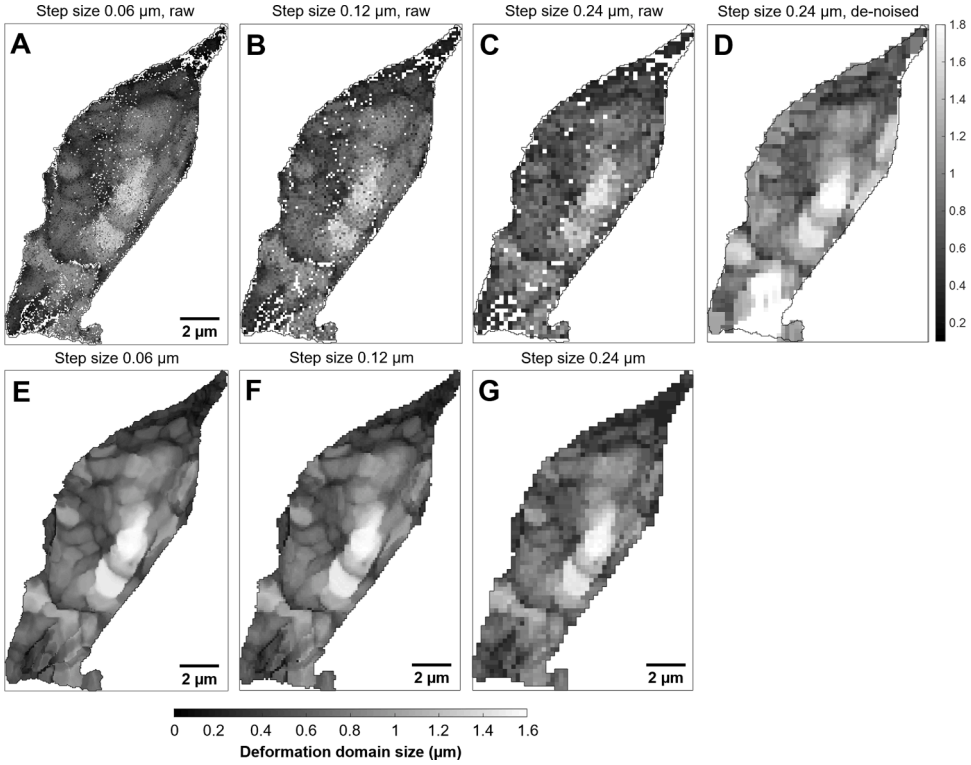

Figure A-5. Deformation domain size for the heavily deformed grain in Indentation 2 at step sizes 0.06 – 0.24 µm: A-C) raw data, D) raw data at 0.24 µm step size after de-noising, shown with a different colour scale (0.1 – 1.8 µm), E-G) data reduced after de-noising the original 0.06 µm dataset.

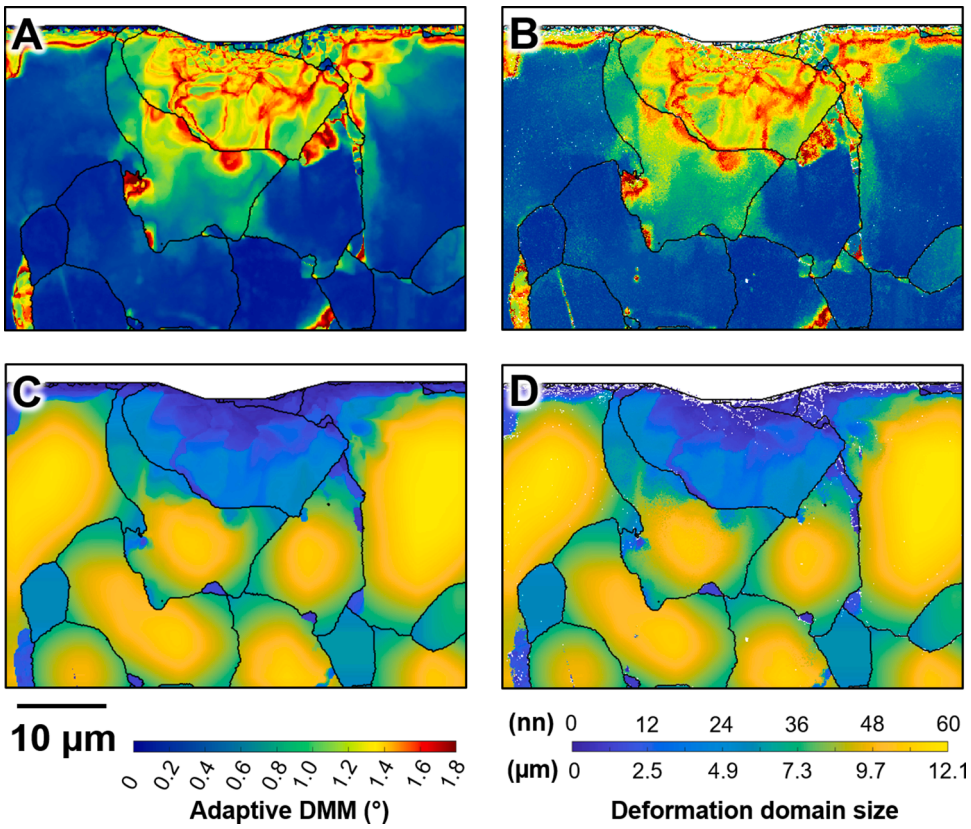

Figure A-6. Comparison of de-noised data (A,C) with raw data (B,D) for Indentation 1 using a kernel size of 60 nearest neighbours; A, B) Adaptive DMM ($\Delta\theta_{SGB}$=2°), C,D) Corresponding deformation domains.

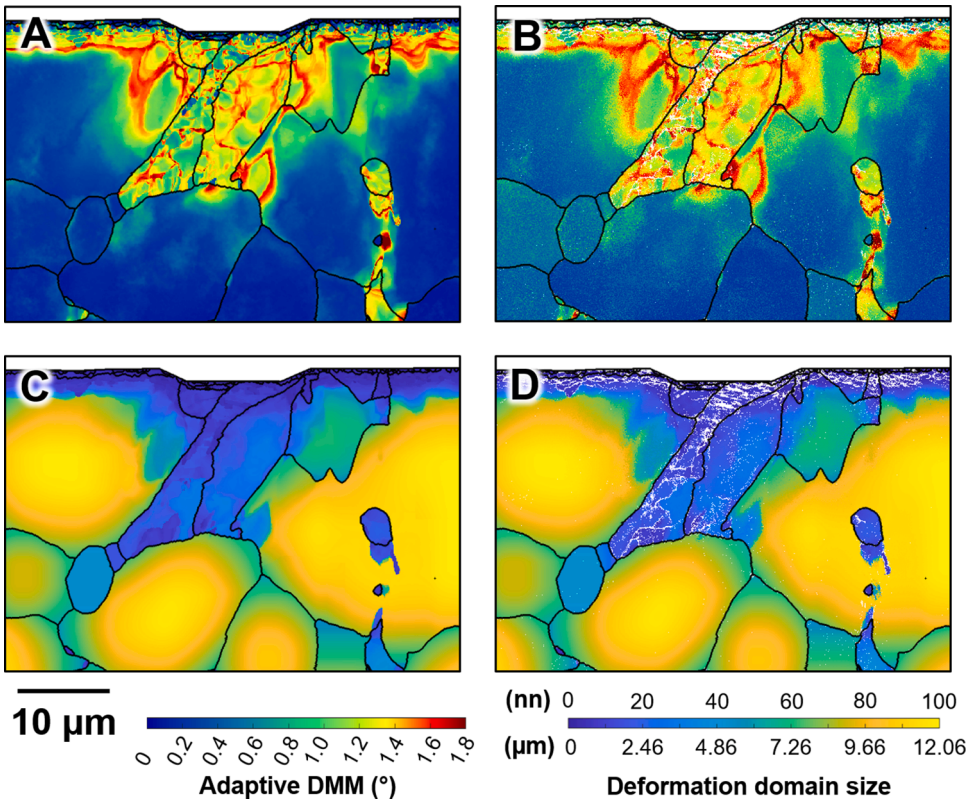

Figure A-7. Comparison of de-noised data (A,C) with raw data (B,D) for Indentation 2 using a kernel size of 100 nearest neighbours; A, B) Adaptive DMM ($\Delta\theta_{SGB}$=2°), C,D) Corresponding deformation domains.

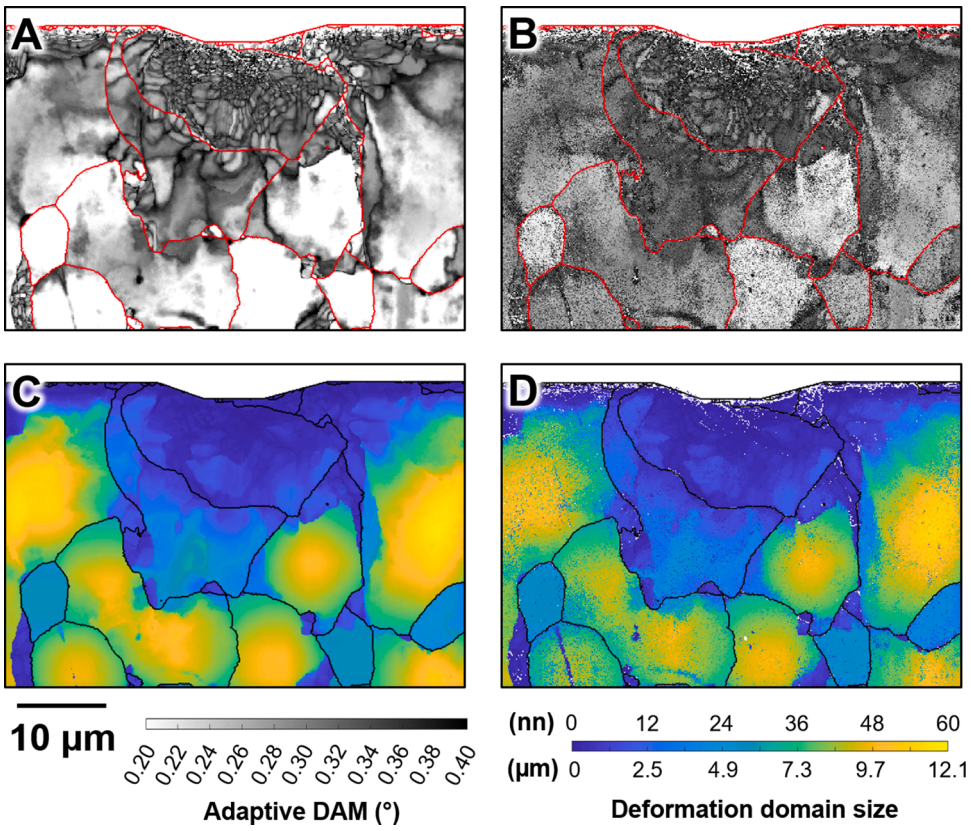

Figure A-8. Comparison of de-noised data (A,C) with raw data (B,D) for Indentation 1 using a kernel size of 60 nearest neighbours; A, B) Adaptive DAM ($\Delta\theta_{DDW}$=0.5°), C,D) Corresponding deformation domains.

measurement noise of 0.37° compared to 0.25° for Indentation 1. It may be caused by the fact that at the smaller step-size the true change in orientation between neighbouring measurement points is smaller, and thus the measurement noise has a larger influence. Still, the half-quadratic filter is able to remove the spatially independent noise extremely well (A, C) with minimal blurring of the features.

The dislocation cell analysis for Indentation 1 is shown in Figure A-8. As only misorientations smaller than 0.5° are considered, the estimated measurement noise of 0.25° is evident for the raw dataset (B) in comparison to the de-noised (A) data. Still, many of the dense dislocation walls can be identified from the raw dataset (B), particularly in the bottom right corner of the heavily deformed grain and the next grain underneath. The deformation domain measurement (C, D) is less affected by the measurement noise in this case as well, with relatively minor speckle patterns visible for raw data (D). A closer inspection of the central grain is shown in Figure A-10, with a large portion of dense dislocation walls and uniform regions inside the dislocation cells resolved for raw data (Figure A-10B). For Indentation 2 shown in Figure A-9, the higher measurement noise of 0.37° is apparent for the raw data (B). As such, the dislocation cells are not well resolved for the highly deformed grain, but similar patterns are observed on both flanks of the indenter as for the de-noised data (A). For the deformation domain measurement, the size is mostly decreased in the undeformed grains using the raw data (D) in comparison to de-noised data (C). The patterns in the deformed volume remain much more similar than would be expected by the noise shown in the adaptive DAM (B). As the highly deformed grain is shown separately in Figure A-10, it is apparent that the dislocation cells are visible from the raw data as well (Figure A-10D). The cumulative probability distributions in Figure 21 show the similarity, even when the spatial resolution is reduced to 0.24 μm. These observations indicate that the half-quadratic de-noising is not introducing artificial features, and that it reduces the spatially independent noise effectively with an acceptable loss in spatial resolution.

Angular resolution for literature datasets

Comparison of sub-grain analysis of the literature datasets (Figure 23) using both de-noised and as-measured raw datasets is shown in Figure A-11. Refer to Table A-1 for estimated measurement noise of all literature datasets. For all datasets the same sub-structural features are resolved, with an expected increase in noise levels for the raw data. This is particularly the case for the Ti-64 Ti-alloy, where the undeformed regions have a similar speckle pattern as seen for Indentation 2. This noise is removed very effectively using the half-quadratic filter. As mentioned before, the A690 Ni-Alloy has extremely low measurement noise, and applying the same filtering parameters as for other datasets makes very little difference to the sub-grain analysis. The deformation domains of the sub-grain and dislocation cell analyses are presented in Figure A-12. The colour scales are chosen to improve contrast of each measurement, with the maximum equivalent value of nearest neighbours shown next to each figure.

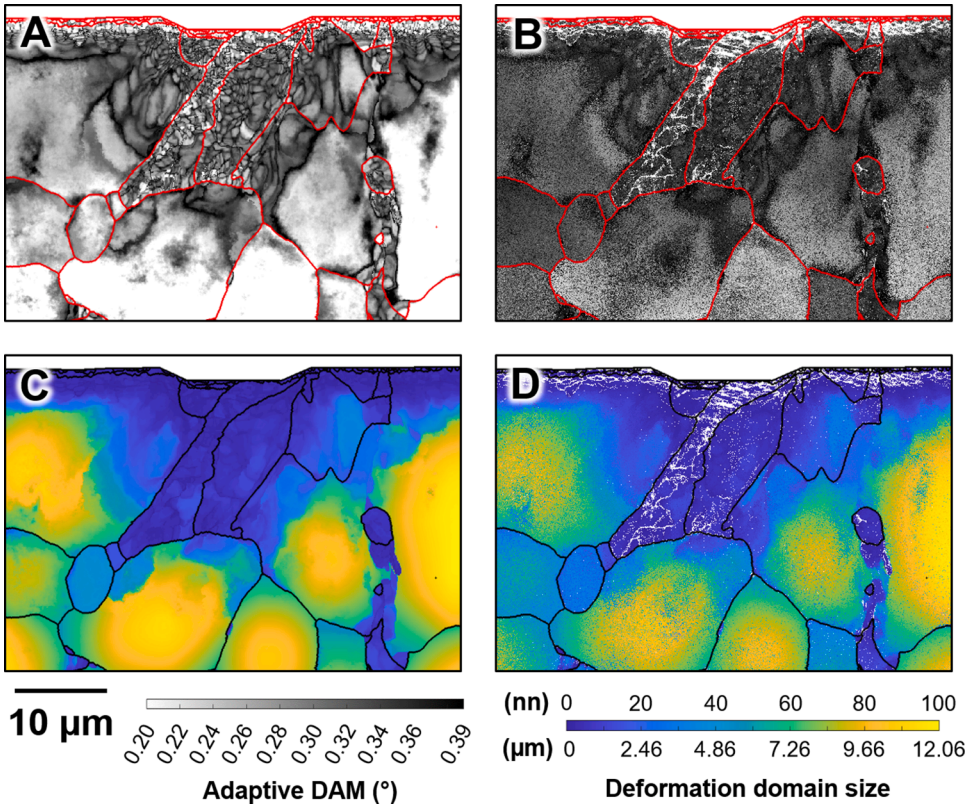

Figure A-9. Comparison of de-noised data (A,C) with raw data (B,D) for Indentation 2 using a kernel size of 100 nearest neighbours; A, B) Adaptive DAM ($\Delta\theta_{DDW}$=*0.5*°), C,D) Corresponding deformation domains.

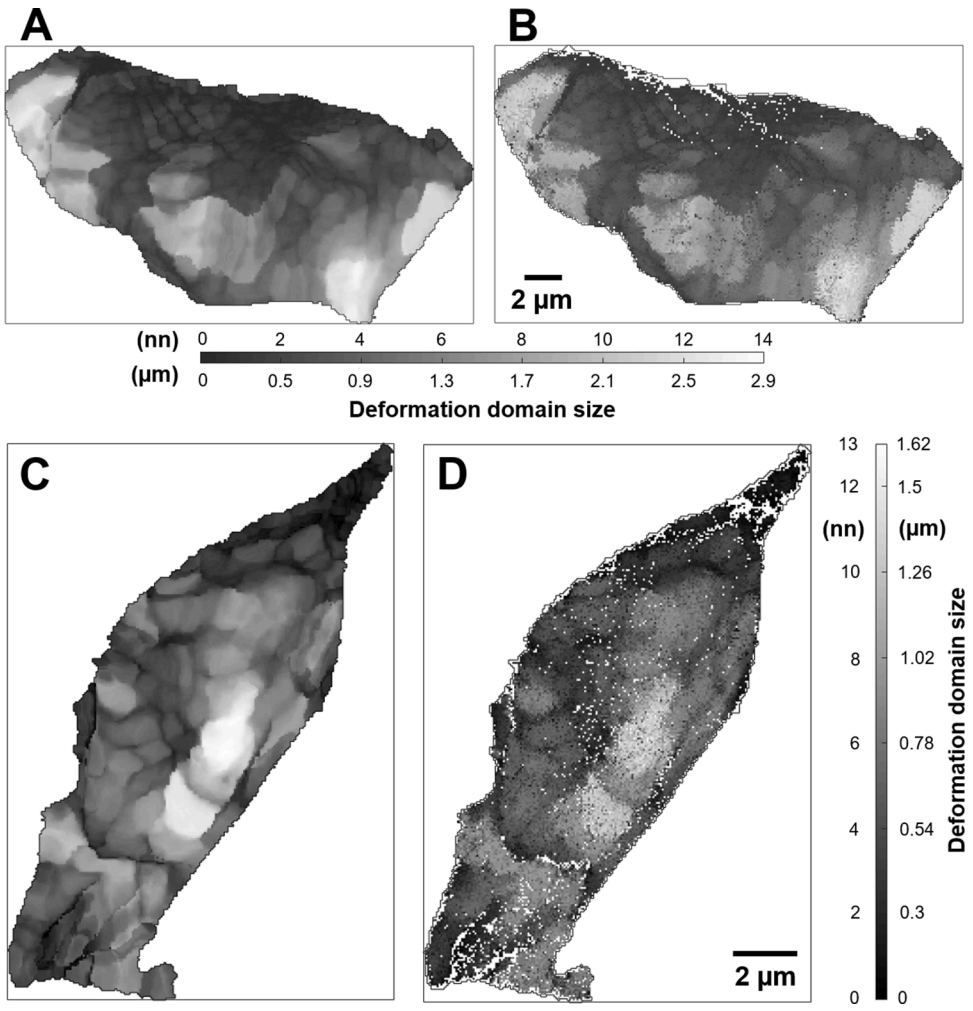

Figure A-10. Deformation domain size for the dislocation cell analysis ($\Delta\theta_{DDW}=0.5^{\circ}$) of heavily deformed grains of Indentation 1 (top) and Indentation 2 (bottom): A,C) The de-noised data, B,D) Raw measurement data. The colour key for Indentation 1 does not extend to deep blacks to better show the details at the top of the grain.

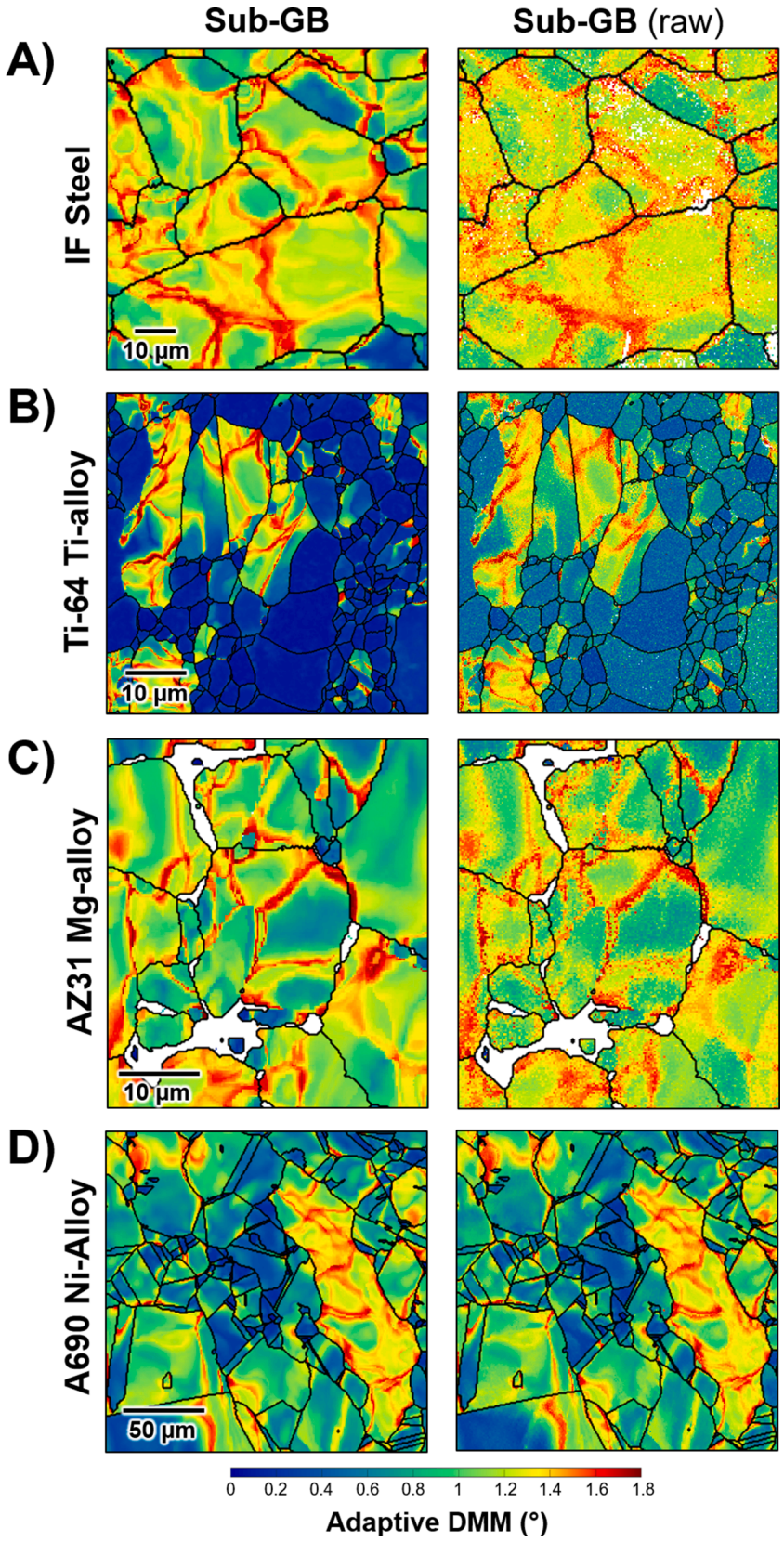

Figure A-11. Comparison of sub-grain analysis for the literature EBSD datasets (Figure 23), showing the adaptive DMM ($\Delta\theta_{SGB}$=2°) for de-noised and raw datasets.

Table A-1
Estimated measurement noise and the global average kernel misorientations for the utilised literature datasets.

	Measurement noise (°)	**Global average KAM, 1st nn (°)**		
Dataset	Raw	Raw	De-noised	De-noising factor
IF steel	0.58	0.64	0.13	5.04
Ti-64 Ti-alloy	0.51	0.56	0.13	4.40
AZ31 Mg-alloy	0.38	0.56	0.11	5.14
A690 Ni-alloy	0.09	0.18	0.10	1.84

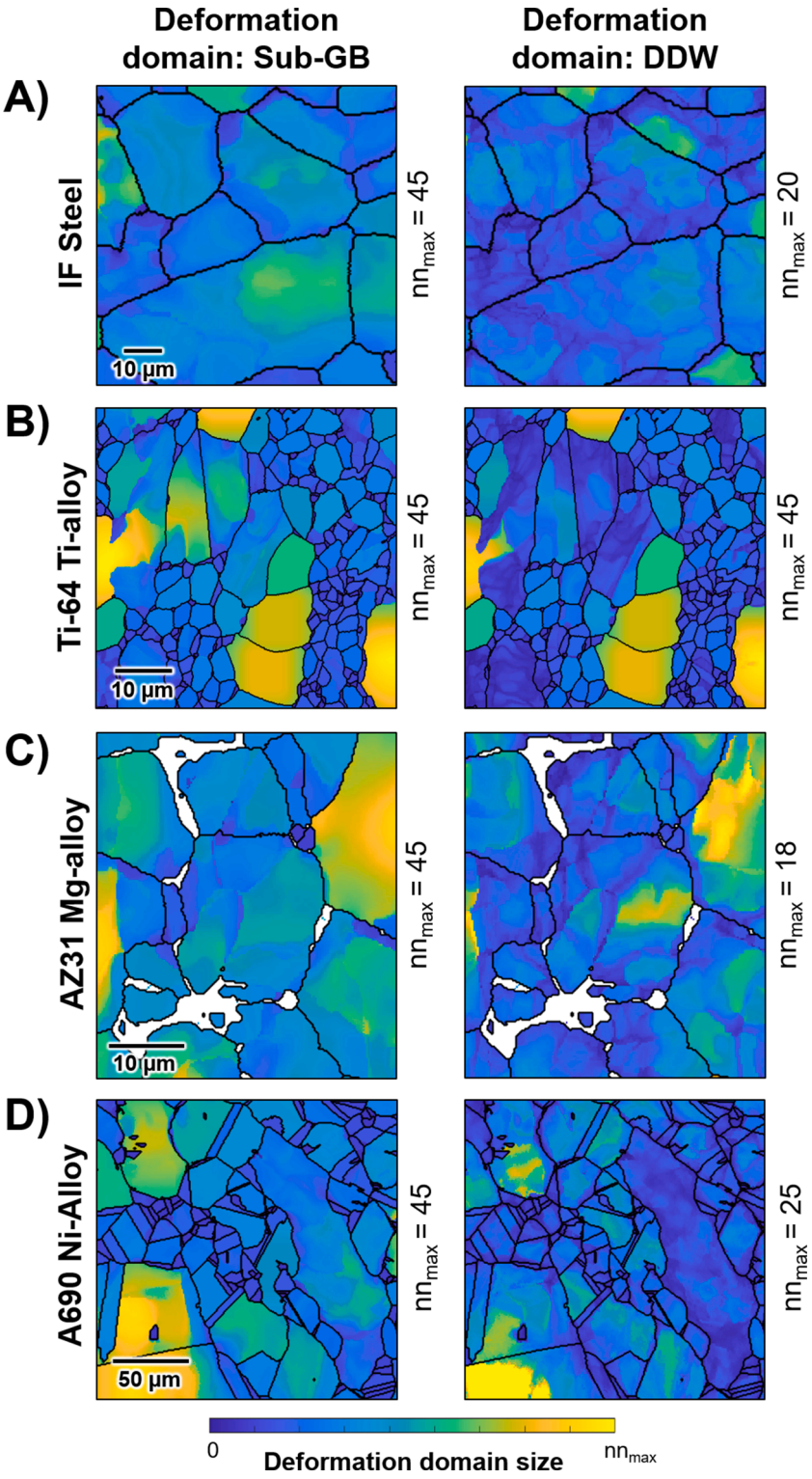

Figure A-12. Deformation domain measurements for the data shown in Figure 23. The colour scale is fixed at 0 – 45 equivalent nearest neighbours for sub-grain boundary analysis ($\Delta\theta_{SGB}=2^{\circ}$) and varies for dense dislocation wall analysis ($\Delta\theta_{DDW}=0.5^{\circ}$) as shown. De-noised data is used for the analyses A-C, and the as-measured raw data for D.

Appendix B. Dislocation cell size measurement

Conventionally the pixel-to-pixel locations of sub-grain boundaries need to be defined in order to measure the size distribution. The results in Section 4.2 indicated that the deformation domain size (Figure 16) measured in the adaptive DAM may represent the dislocation cell size. In order to verify this, the dislocation cell size is measured using the point-sampled linear intercept method [49–51]. The dislocation cells are traced from the adaptive DAM shown in Figure 16B. The measured dislocation cell size is compared to the deformation domain size in Figure B-1B. The volume-weighted average dislocation cell size has very good agreement at 0.76 µm to the average deformation zone size of 0.74

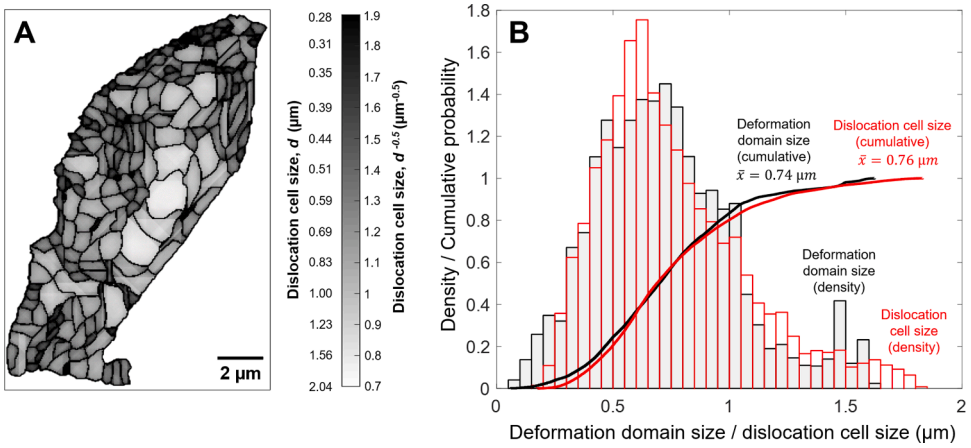

Figure B-1. A) Measurement of dislocation cell size with the locations of DDWs interpreted from Figure 16B, DDWs are overlaid with black colour. The top part of the grain from Figure 16A has been cropped from both analyses as no clear boundaries could be defined. B) Histogram and cumulative probability distributions for the dislocation cell size and the deformation domain size.

μm. Furthermore, the range of values measured and the distribution of the two measurements are very similar. The two discrete peaks in deformation domain size at 1.45 – 1.50 μm and 1.55 – 1.60 μm originate from the two largest dislocation cells, shown by the light grey and white colours in Figure 16A. The most notable difference is observed in the range of 0 – 300 nm, where small deformation domain sizes originate from the dense dislocation walls. Therefore, the presented adaptive domain misorientation approach can reveal the dislocation cells and measure their size distribution simultaneously. Furthermore, the deformation domain size measurement is quite insensitive to spatial resolution for the dislocation cells, as shown in Appendix A. The angular resolution is more important for the dislocation cell analysis, and low measurement noise combined with orientation data de-noising is preferred for accurate measurements.

Appendix C. Kernel size determination for adaptive domain misorientation

The kernel size for the adaptive domain misorientation approach can be determined iteratively by increasing the kernel size, as shown in Figure C-1. At sufficiently large kernel sizes, typically above the average grain size, the measured misorientations start to converge. The convergence can also be estimated from the deformation domain size measurement shown in Figure C-2. As the kernel is sufficiently large, only the central portions of the undeformed grains reach the set kernel size, which in this case is at approximately 60 nearest neighbours or 12.1×12.1 μm. Because of the grain sub-division process, a kernel size of 30 nearest neighbours already starts to be large enough for the highly deformed grain in this case. The Supplementary Video 1 shows the convergence of the measurement between 1 and 100 nearest neighbours in 44 steps for DAM and deformation domain size, including both raw and de-noised datasets.

The iterative process for determining the kernel size can be carried out after the dataset is reduced by 50% or 75% for high spatial resolution datasets, as the deformation domain size measurement is insensitive to spatial resolution as shown in Appendix A. To speed up the iterative process, the kernel sizes can be selected as multiples of the average grain size, e.g. 0.5x, 0.75x, 1x, 1.25x, and so on.

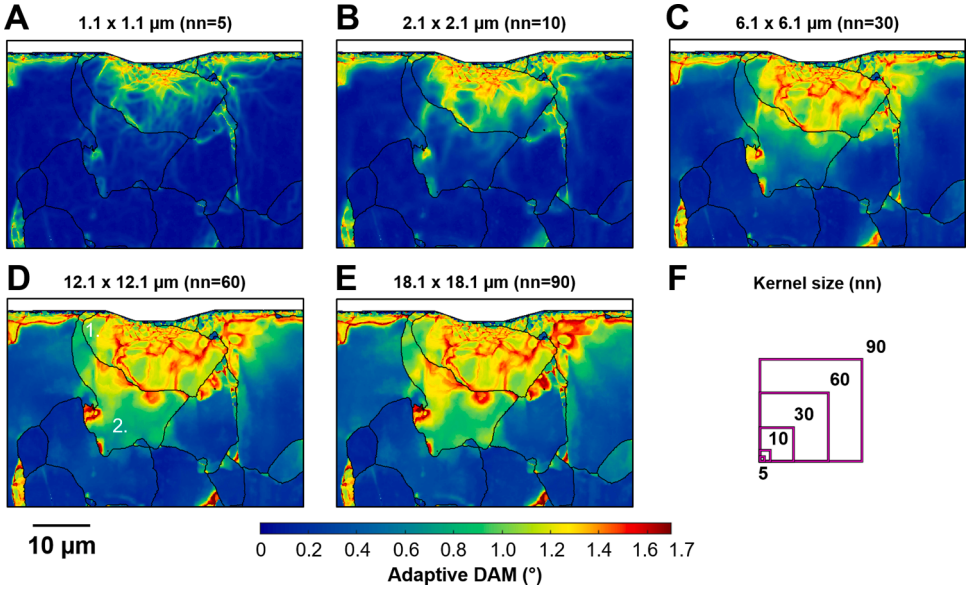

Figure C-1. Adaptive DAM ($\Delta\theta_{SGB}$=2°) with a kernel size between five and ninety nearest neighbours (1.1×1.1 μm – 18.1×18.1 μm), showing convergence of the measurement at sufficiently large kernel sizes.

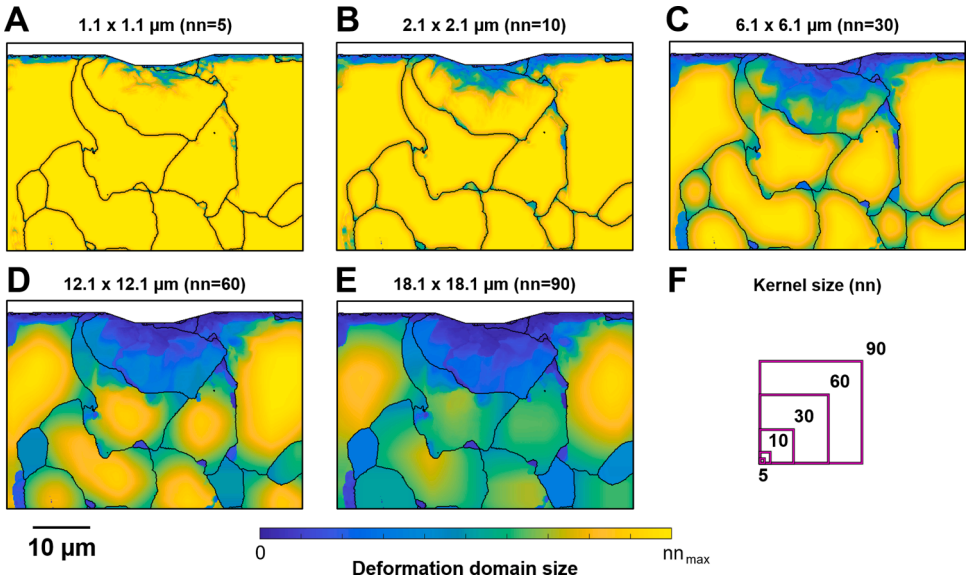

Figure C-2. Deformation domain ($\Delta\theta_{SGB}$=2°) with a kernel size between five and ninety nearest neighbours (1.1×1.1 µm – 18.1×18.1 µm), showing convergence of the measurement at sufficiently large kernel sizes.

References

[1] S. Sun, B.L. Adams, W.E. King, Observations of lattice curvature near the interface of a deformed aluminium bicrystal, Philos. Mag. A Phys. Condens. Matter, Struct. Defects Mech. Prop. 80 (2000) 9–25, https://doi.org/10.1080/01418610008212038.

[2] J.F. Nye, Some geometrical relations in dislocated crystals, Acta Metall 1 (1953) 153–162, https://doi.org/10.1016/0001-6160(53)90054-6.

[3] E. Kröner, Continuum Theory of Dislocation and Self-Stresses, Springer-Verlag, Berlin, 1953.

[4] B.A. Bilby, R. Bullough, E. Smith, Continuous distributions of dislocations: New application of the methods of non-Riemannian geometry, Proc. Roy. Soc. L. 231 (1955) 263–273.

[5] M.F. Ashby, The deformation of plastically non-homogeneous materials, Philos. Mag. 21 (1970) 399–424.

[6] S.V Harren, H.E. Dève, R.J. Asaro, Shear band formation in plane strain compression, Acta Metall 36 (1988) 2435–2480, https://doi.org/10.1016/0001-6160(88)90193-9.

[7] R. Becker, S. Panchanadeeswaran, Effects of grain interactions on deformation and local texture in polycrystals, Acta Metall. Mater. 43 (1995).

[8] L.S. Tóth, Y. Estrin, R. Lapovok, C. Gu, A model of grain fragmentation based on lattice curvature, Acta Mater 58 (2010) 1782–1794, https://doi.org/10.1016/j.actamat.2009.11.020.

[9] J.D. Eshelby, F.C. Frank, F.R.N. Nabarro, The equilibrium of linear arrays of dislocations, London, Edinburgh, Dublin Philos. Mag. J. Sci. 42 (1951) 351–364, https://doi.org/10.1080/14786445108561060.

[10] E.O. Hall, The deformation and ageing of mild steel: III Discussion of results, Proc. Phys. Soc. B. 64 (1951) 747–753.

[11] N.J. Petch, The cleavage strength of polycrystals, J. Iron Steel Inst. 174 (1953) 25–28.

[12] R.W. Armstrong, 60 Years of Hall-Petch: Past to Present Nano-Scale Connections, Mater. Trans. 55 (2014) 2–12, https://doi.org/10.2320/matertrans.MA201302.

[13] O. Muránsky, L. Balogh, M. Tran, C.J. Hamelin, J.S. Park, M.R. Daymond, On the measurement of dislocations and dislocation substructures using EBSD and HRSD techniques, Acta Mater 175 (2019) 297–313, https://doi.org/10.1016/j.actamat.2019.05.036.

[14] N.R. Tao, Z.B. Wang, W.P. Tong, M.L. Sui, J. Lu, K. Lu, An investigation of surface nanocrystallization mechanism in Fe induced by surface mechanical attrition treatment, Acta Mater 50 (2002) 4603–4616, https://doi.org/10.1016/S1359-6454(02)00310-5.

[15] J. Lu, L. Hultman, E. Holmström, K.H. Antonsson, M. Grehk, W. Li, L. Vitos, A. Golpayegani, Stacking fault energies in austenitic stainless steels, Acta Mater 111 (2016) 39–46, https://doi.org/10.1016/j.actamat.2016.03.042.

[16] P. Landau, R.Z. Shneck, G. Makov, A. Venkert, Evolution of dislocation patterns in fcc metals, IOP Conf. Ser. Mater. Sci. Eng. (2009) 3, https://doi.org/10.1088/1757-899X/3/1/012004.

[17] K. Wang, N.R. Tao, G. Liu, J. Lu, K. Lu, Plastic strain-induced grain refinement at the nanometer scale in copper, Acta Mater 54 (2006) 5281–5291, https://doi.org/10.1016/j.actamat.2006.07.013.

[18] X. Wu, N. Tao, Y. Hong, B. Xu, J. Lu, K. Lu, Microstructure and evolution of mechanically-induced ultrafine grain in surface layer of AL-alloy subjected to USSP, Acta Mater 50 (2002) 2075–2084, https://doi.org/10.1016/S1359-6454(02)00051-4.

[19] J.C. Tan, M.J. Tan, Dynamic continuous recrystallization characteristics in two stage deformation of Mg-3Al-1Zn alloy sheet, Mater. Sci. Eng. A. 339 (2003) 124–132, https://doi.org/10.1016/S0921-5093(02)00096-5.

[20] A. Das, S. Sivaprasad, P.C. Chakraborti, S. Tarafder, Connection between deformation-induced dislocation substructures and martensite formation in stainless steel, Philos. Mag. Lett. 91 (2011) 664–675, https://doi.org/10.1080/09500839.2011.608385.

[21] I. Gutierrez-Urrutia, D. Raabe, Dislocation and twin substructure evolution during strain hardening of an Fe-22 wt.% Mn-0.6 wt.% C TWIP steel observed by electron channeling contrast imaging, Acta Mater 59 (2011) 6449–6462, https://doi.org/10.1016/j.actamat.2011.07.009.

[22] D. Kuhlmann-Wilsdorf, Theory of plastic deformation: - properties of low energy dislocation structures, Mater. Sci. Eng. A. 113 (1989) 1–41, https://doi.org/10.1016/0921-5093(89)90290-6.

[23] R.Z. Valiev, R.K. Islamgaliev, I. V. Alexandrov, Bulk nanostructured materials from severe plastic deformation, 2000. https://doi.org/10.1016/S0079-6425(99)00007-9.

[24] P. Rolland, K. Dicks, R. Ravel-Chapuis, EBSD Spatial Resolution in the SEM when Analyzing Small Grains or Deformed Material, Microsc. Microanal. 8 (2002) 670–671, https://doi.org/10.1017/s1431927602106350.

[25] M.D. Sangid, T. Ezaz, H. Sehitoglu, I.M. Robertson, Energy of slip transmission and nucleation at grain boundaries, Acta Mater 59 (2011) 283–296, https://doi.org/10.1016/j.actamat.2010.09.032.

[26] W.Z. Abuzaid, M.D. Sangid, J.D. Carroll, H. Sehitoglu, J. Lambros, Slip transfer and plastic strain accumulation across grain boundaries in Hastelloy X, J. Mech. Phys. Solids. 60 (2012) 1201–1220, https://doi.org/10.1016/j.jmps.2012.02.001.

[27] D. Wilson, W. Wan, F.P.E. Dunne, Microstructurally-sensitive fatigue crack growth in HCP, BCC and FCC polycrystals, J. Mech. Phys. Solids. 126 (2019) 204–225, https://doi.org/10.1016/j.jmps.2019.02.012.

[28] F. Di Gioacchino, J.Quinta Da Fonseca, An experimental study of the polycrystalline plasticity of austenitic stainless steel, Int. J. Plast. 74 (2015) 92–109, https://doi.org/10.1016/j.ijplas.2015.05.012.

[29] R.A. Schwarzer, Spatial Resolution in ACOM - What Will Come After EBSD, Micros. Today. 16 (2018) 34–37, https://doi.org/10.1017/s1551929500054316.

[30] T. Maitland, S. Sitzman, Electron Backscatter Diffraction (EBSD) Technique and Materials Characterization Examples, in: W. Zhou, Z.L. Wang (Eds.), Electron Backscatter Diffraction (EBSD) Technique and Materials Characterization Examples, Scanning Microsc. Nanotechnol. (2007) 41–76, https://doi.org/10.1007/978-0-387-39620-0.

[31] S.I. Wright, M.M. Nowell, D.P. Field, A review of strain analysis using electron backscatter diffraction, Microsc. Microanal. 17 (2011) 316–329, https://doi.org/10.1017/S1431927611000055.

[32] M. Kamaya, A.J. Wilkinson, J.M. Titchmarsh, Quantification of plastic strain of stainless steel and nickel alloy by electron backscatter diffraction, Acta Mater 54 (2006) 539–548, https://doi.org/10.1016/j.actamat.2005.08.046.

[33] C. McMahon, B. Soe, A. Loeb, A. Vemulkar, M. Ferry, L. Bassman, Ultramicroscopy Boundary identi fi cation in EBSD data with a generalization of fast multiscale clustering, Ultramicroscopy 133 (2013) 16–25, https://doi.org/10.1016/j.ultramic.2013.04.009.

[34] S.S. Rui, L.S. Niu, H.J. Shi, S. Wei, C.C. Tasan, Diffraction-based misorientation mapping: A continuum mechanics description, J. Mech. Phys. Solids. (2019) 133, https://doi.org/10.1016/j.jmps.2019.103709.
[35] M. Kamaya, Assessment of local deformation using EBSD: Quantification of accuracy of measurement and definition of local gradient, Ultramicroscopy 111 (2011) 1189–1199, https://doi.org/10.1016/j.ultramic.2011.02.004.
[36] A.D. Rollett, F. Wagner, N. Allain-Bonasso, D.P. Field, R.a. Lebensohn, Comparison of Gradients in Orientation and Stress between Experiment and Simulation, Mater. Sci. Forum. 702–703 (2011) 463–468, https://doi.org/10.4028/www.scientific.net/MSF.702-703.463.
[37] F.J. Humphreys, P.S. Bate, P.J. Hurley, Orientation averaging of electron backscattered diffraction data, J. Microsc. 201 (2001) 50–58, https://doi.org/10.1046/j.1365-2818.2001.00777.x.
[38] R. Bergmann, R.H. Chan, R. Hielscher, J. Persch, G. Steidl, Restoration of manifold-valued images by half-quadratic minimization, Inverse Probl. Imaging. 10 (2016) 281–304, https://doi.org/10.3934/ipi.2016001.
[39] R. Kilian, R. Heilbronner, Analysis of crystallographic preferred orientations of experimentally deformed Black Hills Quartzite, Solid Earth 8 (2017) 1095–1117, https://doi.org/10.5194/se-2017-44.
[40] R. Hielscher, C.B. Silbermann, E. Schmidla, J. Ihlemannb, Denoising of crystal orientation maps, J. Appl. Crystallogr. 52 (2019) 984–996, https://doi.org/10.1107/S1600576719009075.
[41] A. Seret, C. Moussa, M. Bernacki, J. Signorelli, N. Bozzolo, Estimation of geometrically necessary dislocation density from filtered EBSD data by a local linear adaptation of smoothing splines, J. Appl. Crystallogr. 52 (2019) 548–563, https://doi.org/10.1107/S1600576719004035.
[42] G.E. Lloyd, A.B. Farmer, D. Mainprice, Misorientation analysis and the formation and orientation of subgrain and grain boundaries, Tectonophysics 279 (1997) 55–78, https://doi.org/10.1016/S0040-1951(97)00115-7.
[43] W. Pantleon, Formation of disorientations in dislocation structures during plastic deformation, 2002, https://doi.org/10.4028/www.scientific.net/ssp.87.73.
[44] Y. Estrin, L.S. Tóth, Y. Brechet, H.S. Kim, Modelling of the evolution of dislocation cell misorientation under severe plastic deformation, 2006, https://doi.org/10.4028/0-87849-985-7.675.
[45] D. Kiener, K. Durst, M. Rester, A.M. Minor, Revealing deformation mechanisms with nanoindentation, Jom 61 (2009) 14–23, https://doi.org/10.1007/s11837-009-0036-4.
[46] P. Lehto, Grain interaction in local plastic deformation of welded structural steel - Influence of length-scale on sub-grain deformation behaviour for polycrystalline BCC material, Aalto University, 2019 http://urn.fi/URN:ISBN:978-952-60-8807-5.
[47] D. Kiener, R. Pippan, C. Motz, H. Kreuzer, Microstructural evolution of the deformed volume beneath microindents in tungsten and copper, Acta Mater 54 (2006) 2801–2811, https://doi.org/10.1016/j.actamat.2006.02.024.
[48] A. Wilkinson, G. Meaden, D.J. Dingley, High resolution mapping of strains and rotations using electron backscatter diffraction, Mater. Sci. Technol. 22 (2006) 1271–1278, https://doi.org/10.1179/174328406×130966.
[49] P. Lehto, H. Remes, T. Saukkonen, H. Hänninen, J. Romanoff, Influence of grain size distribution on the Hall-Petch relationship of welded structural steel, Mater. Sci. Eng. A. (2014) 592, https://doi.org/10.1016/j.msea.2013.10.094.
[50] P. Lehto, J. Romanoff, H. Remes, T. Sarikka, Characterisation of local grain size variation of welded structural steel, Weld. World. 60 (2016) 673–688, https://doi.org/10.1007/s40194-016-0318-8.
[51] P. Lehto, Aalto University Wiki - Grain size measurement using Matlab, 2017. https://wiki.aalto.fi/display/GSMUM.
[52] W.J. Cheong, B.L. Luan, D.W. Shoesmith, The effects of stabilizers on the bath stability of electroless Ni deposition and the deposit, Appl. Surf. Sci. 229 (2004) 282–300, https://doi.org/10.1016/j.apsusc.2004.02.003.
[53] P. Lehto, Aalto University Wiki - EBSD measurement of deformation induced dislocation sub-structures, 2021. https://wiki.aalto.fi/display/EMDIDS.
[54] T. Britton, D. Goran, V.S. Tong, Space rocks and optimising scanning electron channelling contrast, Mater. Charact. 142 (2018) 422–431, https://doi.org/10.1016/j.matchar.2018.06.001.
[55] F. Bachmann, R. Hielscher, H. Schaeben, Texture analysis with MTEX- Free and open source software toolbox, Solid State Phenom.Mater. Charact.w 160 (2010) 63–68, https://doi.org/10.4028/www.scientific.net/SSP.160.63.
[56] G. Nolze, R. Hielscher, IPF coloring of crystal orientation data, J. Appl. Crystallogr. (2016). http://mtex-toolbox.github.io/publications.html.
[57] P. Lehto, EBSD datasets for cross-sectioned structural steel hardness indentations, 2021, https://doi.org/10.5281/zenodo.4430628.
[58] P. Lehto, Adaptive domain misorientation approach for the EBSD measurement of deformation induced dislocation sub-structures, 2021, https://doi.org/10.5281/zenodo.4430624.
[59] B. Britton, J. Hickey, Example MTEX EBSD data from Iron, 2018, https://doi.org/10.5281/ZENODO.1434868.
[60] B. Britton, V. Tong, D. Dye, A. Knowles, Data Bundle for "Rapid electron backscatter diffraction mapping: Painting by numbers, 2018, https://doi.org/10.5281/ZENODO.1488072.
[61] V.S. Tong, A.J. Knowles, D. Dye, T.Ben Britton, Rapid electron backscatter diffraction mapping: Painting by numbers, Mater. Charact. 147 (2019) 271–279, https://doi.org/10.1016/j.matchar.2018.11.014.
[62] A. Orozco-Caballero, J.Q. da Fonseca, EBSD data for HRDIC analysis in AZ31, 2017, https://doi.org/10.5281/ZENODO.345925.
[63] A. Orozco-Caballero, D. Lunt, J.D. Robson, J. Quinta da Fonseca, How magnesium accommodates local deformation incompatibility: A high-resolution digital image correlation study, Acta Mater 133 (2017) 367–379, https://doi.org/10.1016/j.actamat.2017.05.040.
[64] A. Orozco-Caballero, J.Q. da Fonseca, Magnesium AZ31 HRDIC Data Set, 2017, https://doi.org/10.5281/ZENODO.345313.
[65] A. Harte, M. Atkinson, A. Smith, C. Drouven, S. Zaefferer, J. Quinta da Fonseca, M. Preuss, The effect of solid solution and gamma prime on the deformation modes in Ni-based superalloys, Acta Mater 194 (2020) 257–275, https://doi.org/10.1016/j.actamat.2020.04.004.
[66] A. Harte, M. Atkinson, M. Preuss, J.Q. da Fonseca, High resolution deformation data from the surface of a Nickel-based alloy: Solid solution, 2020, https://doi.org/10.5281/ZENODO.3691937.
[67] R.R. Shen, P. Efsing, Overcoming the drawbacks of plastic strain estimation based on KAM, Ultramicroscopy 184 (2018) 156–163, https://doi.org/10.1016/j.ultramic.2017.08.013.
[68] G. Nolze, R. Hielscher, A. Winkelmann, Electron backscatter diffraction beyond the mainstream, Cryst. Res. Technol. 52 (2017) 1–24, https://doi.org/10.1002/crat.201600252.
[69] G. Nolze, M. Jürgens, J. Olbricht, A. Winkelmann, Improving the precision of orientation measurements from technical materials via EBSD pattern matching, Acta Mater 159 (2018) 408–415, https://doi.org/10.1016/j.actamat.2018.08.028.
[70] A. Winkelmann, G. Cios, T. Tokarski, G. Nolze, R. Hielscher, T. Kozieł, EBSD orientation analysis based on experimental Kikuchi reference patterns, Acta Mater 188 (2020) 376–385, https://doi.org/10.1016/j.actamat.2020.01.053.
[71] S. Singh, M. De Graef, Dictionary indexing of electron channeling patterns, Microsc. Microanal. 23 (2017) 1–10, https://doi.org/10.1017/S1431927616012769.
[72] W.C. Lenthe, S. Singh, M. De Graef, A spherical harmonic transform approach to the indexing of electron back-scattered diffraction patterns, Ultramicroscopy 207 (2019), 112841, https://doi.org/10.1016/j.ultramic.2019.112841.
[73] A. Gholinia, P.B. Prangnell, M.V. Markushev, Effect of strain path on the development of deformation structures in severely deformed aluminium alloys processed by ECAE, Acta Mater 48 (2000) 1115–1130, https://doi.org/10.1016/S1359-6454(99)00388-2.
[74] S.C. Baik, Y. Estrin, H.S. Kim, R.J. Hellmig, Dislocation density-based modeling of deformation behavior of aluminium under equal channel angular pressing, Mater. Sci. Eng. A. 351 (2003) 86–97, https://doi.org/10.1016/S0921-5093(02)00847-X.
[75] F.J. Humphreys, Reconstruction of grains and subgrains from electron backscatter diffraction maps, J. Microsc. 213 (2004) 247–256, https://doi.org/10.1111/j.0022-2720.2004.01297.x.
[76] T.J. Ruggles, Y.S.J. Yoo, B.E. Dunlap, M.A. Crimp, J. Kacher, Correlating results from high resolution EBSD with TEM- and ECCI-based dislocation microscopy: Approaching single dislocation sensitivity via noise reduction, Ultramicroscopy 210 (2020), 112927, https://doi.org/10.1016/j.ultramic.2019.112927.
[77] D. Wallis, A.J. Parsons, L.N. Hansen, Quantifying geometrically necessary dislocations in quartz using HR-EBSD: Application to chessboard subgrain boundaries, J. Struct. Geol. 125 (2019) 235–247, https://doi.org/10.1016/j.jsg.2017.12.012.
[78] I. Weikusat, E.J.N. Kuiper, G.M. Pennock, S. Kipfstuhl, M.R. Drury, EBSD analysis of subgrain boundaries and dislocation slip systems in Antarctic and Greenland ice, Solid Earth 8 (2017) 883–898, https://doi.org/10.5194/se-8-883-2017.
[79] T. Chauve, M. Montagnat, F. Barou, K. Hidas, A. Tommasi, D. Mainprice, Investigation of nucleation processes during dynamic recrystallization of ice using cryo-EBSD, Philos. Trans. R. Soc. A Math. Phys. Eng. Sci. (2017) 375, https://doi.org/10.1098/rsta.2015.0345.